PHYSICAL REVIEW D **79,** 084011 (2009)

Strategies for the characteristic extraction of gravitational waveforms

M. C. Babiuc,[1] N. T. Bishop,[2] B. Szilágyi,[3,4] and J. Winicour[3,5]

[1]*Department of Physics, Marshall University, Huntington, West Virginia 25755, USA*
[2]*Department of Mathematical Sciences, University of South Africa, Unisa 0003, South Africa*
[3]*Max-Planck-Institut für Gravitationsphysik, Albert-Einstein-Institut, 14476 Golm, Germany*
[4]*Theoretical Astrophysics, California Institute of Technology, Pasadena, California 91125, USA*
[5]*Department of Physics and Astronomy, University of Pittsburgh, Pittsburgh, Pennsylvania 15260, USA*

(Received 6 August 2008; published 7 April 2009)

We develop, test, and compare new numerical and geometrical methods for improving the accuracy of extracting waveforms using characteristic evolution. The new numerical method involves use of circular boundaries to the stereographic grid patches which cover the spherical cross sections of the outgoing null cones. We show how an angular version of numerical dissipation can be introduced into the characteristic code to damp the high frequency error arising form the irregular way the circular patch boundary cuts through the grid. The new geometric method involves use of the Weyl tensor component Ψ_4 to extract the waveform as opposed to the original approach via the Bondi news function. We develop the necessary analytic and computational formula to compute the $O(1/r)$ radiative part of Ψ_4 in terms of a conformally compactified treatment of null infinity. These methods are compared and calibrated in test problems based upon linearized waves.

DOI: 10.1103/PhysRevD.79.084011 PACS numbers: 04.20.Jb, 04.25.Nx, 04.30.Db, 04.70.Bw

I. INTRODUCTION

The unambiguous geometric description of gravitational radiation in curved spacetimes traces back to the work of Bondi [1] *et al.*, Sachs [2], and Penrose [3]. By formulating asymptotic flatness in terms of characteristic hypersurfaces extending to infinity, they were able to reconstruct, in a nonlinear geometric setting, the basic properties of gravitational waves which had been developed in linearized theory on a Minkowski background. The major new nonlinear features were the Bondi mass and news function, and the mass loss formula relating them. This approach has been implemented as a characteristic evolution code [4,5] which computes the radiation field at infinity by using a Penrose compactification of the space-time. The code computes the gravitational radiation reaching infinity in terms of boundary data supplied on an inner worldtube. This has timely application to the important astrophysical problem of the inspiral and merger of a binary black hole. Several Cauchy codes, using an artificial outer boundary condition, are now able to simulate this binary problem. By using the data on a worldtube carved out of these binary black hole spacetimes obtained by Cauchy evolution, the characteristic code can supply the resulting waveform at infinity. In this work, we develop and test new methods designed to enhance the accuracy of this approach to computing gravitational waveforms, which has been called *Cauchy-characteristic extraction* (CCE) [6].

The Cauchy codes presently being applied to the binary black hole problem introduce an artificial outer boundary, where some boundary condition must be employed. The choice of the proper boundary condition for an isolated radiating system is a global problem, which can only be treated exactly by an extension of the solution to infinity, e.g. by conformal compactification. The most elegant such approach is the extension of the Cauchy problem to future null infinity $\mathcal{I}^+$ by means of a hyperboloidal time foliation [7] (see [8,9] for reviews of progress in this direction). Another approach is to extend the solution to $\mathcal{I}^+$ by matching the interior Cauchy evolution to an exterior characteristic evolution, i.e. Cauchy-characteristic matching (CCM) [10]. (see [11] for a review). CCM has been applied successfully to gravitational wave computations in the linear regime [12] but has not yet been extended to the nonlinear binary black hole problem.

When an artificial finite outer boundary is introduced there are two broad sources of error:

(i) The outer boundary condition
(ii) Waveform extraction at an inner worldtube.

The first source of error stems from the outer boundary condition, which must lead to a well-posed constraint-preserving initial-boundary value problem. This has not yet been fully established for any of the present black hole codes. But, even were such boundary conditions implemented, the correct boundary data must be prescribed. However, this boundary data can only be exactly determined, in general, by extending the solution to infinity [13]. Otherwise, the best that can be done is to impose a boundary condition for which *homogeneous* boundary data, i.e. zero boundary values, is a good approximation. One proposal of this type [14] is a boundary condition that requires the Newman-Penrose [15] Weyl tensor component Ψ_0 to vanish. In the limit that the outer boundary goes to infinity this outer boundary condition becomes exact. In the present state of the art of black hole simulations, this approach comes closest to a satisfactory treatment of the outer boundary [16].

 © 2009 The American Physical Society

The second source of error arises from waveform extraction at an inner worldtube, which must be well inside the outer boundary in order to isolate it from errors introduced by the boundary condition. There the waveform is typically extracted by a perturbative scheme based upon the introduction of a background Schwarzschild spacetime. This has been carried out using the Regge-Wheeler-Zerilli [17,18] treatment of the perturbed metric, as reviewed in [19], and also by calculating the Newman-Penrose Weyl component Ψ_4, as first done for the binary black hole problem in [20–23]. In this approach, errors arise from the finite size of the extraction worldtube, from nonlinearities and from gauge ambiguities involved in the arbitrary introduction of a background metric. The gauge ambiguities might seem less severe in the case of Ψ_4 (vs metric) extraction, but there are still delicate problems associated with the choices of a preferred null tetrad and preferred worldlines along which to measure the waveform (see [24] for an analysis).

Cauchy-characteristic extraction, which is one of the pieces of the CCM strategy, offers a means to avoid this error introduced by extraction at a finite worldtube. In CCE, the inner worldtube data supplied by the Cauchy evolution is used as boundary data for a characteristic evolution to future null infinity, where the waveform can be unambiguously computed by geometric methods. By itself, CCE does not use the characteristic evolution to inject outer boundary data for the Cauchy evolution, which can be a source of instability in full CCM. Highly nonlinear tests in black hole spacetimes [5] have shown that characteristic evolution is a stable procedure which provides the geometry in the neighborhood of null infinity up to numerical error; and tests in the perturbative regime [25] show that CCE compares favorably with Zerilli extraction and has advantages at small extraction radii. However, in astrophysically realistic cases which require high resolution, such as the inspiral of matter into a black hole [26], this error has been a troublesome factor in the postprocessing of the numerical solution which is necessary to compute the asymptotic quantities determining the Bondi news function.

There are two distinct ways, geometric and numerical, that the accuracy of this calculation of the gravitational waveform might be improved. In the geometrical category, one option is to compute Ψ_4 instead of the news function as the primary description of the waveform. We discuss this in Sec. III, where we develop the extensive formulas necessary to compute the asymptotic $O(1/r)$ part of Ψ_4, i.e. $\Psi_4^0 = \lim_{r\to\infty} r\Psi_4$, which governs the radiation.

In the numerical category, some standard methods for improving accuracy, such as higher order finite difference approximations, would be easy to implement whereas others, such as adaptive mesh refinement, have only been tackled for 1D characteristic codes [27]. But beyond these methods, a major source of error in characteristic evolution arises from the intergrid interpolations arising from the multiple patches necessary to coordinatize smoothly the spherical cross sections of the outgoing null hypersurfaces. The development of grids smoothly covering the sphere has had a long history in computational meteorology that has led to two distinct approaches: (i) the stereographic approach in which the sphere is covered by two overlapping patches obtained by stereographic projection about the North and South poles [28]; and (ii) the cubed-sphere approach in which the sphere is covered by the 6 patches obtained by a projection of the faces of a circumscribed cube [29]. Recently, the cubed-sphere approach has received much attention because the simple structure of its shared boundaries allows a highly scalable algorithm for parallel architectures. A discussion of the advantages of each of these methods and a comparison of their performance in a standard fluid test bed are given in [28]. In numerical relativity, the stereographic method has been reinvented in the context of the characteristic evolution problem [30]; and the cubed-sphere method reinvented in the context of building an apparent horizon finder [31]. The characteristic evolution code was first developed using two square stereographic patches, each overlapping the equator. We consider here a modification, based upon the approach advocated in [28], which retains the original stereographic patch structure but shrinks the overlap region by masking a circular boundary near the equator. Recently, the cubed-sphere method has also been developed for application to characteristic evolution [32,33].

These geometric and numerical considerations lead to four options for improving CCE:

(i) Computation of the news function using circular stereographic patches
(ii) Computation of the Weyl tensor using circular stereographic patches
(iii) Computation of the news function using the cubed-sphere patching
(iv) Computation of the Weyl tensor using cubed-sphere patching

We compare these options here in the context of model problems designed to test their application to CCE. Because the cubed-sphere approach requires further code development to be applied to CCE, in Sec. V we present a test based upon the propagation of a wave on the sphere to provide a preliminary comparison with the stereographic approach. The test compares their accuracy in calculating the angular derivatives required in the news and Weyl tensor extraction algorithms. In Sec. VI, we next present tests of CCE which compare the news and Weyl tensor approaches in a linearized gravitational wave test problem.

The development of finite-difference evolution algorithms, which was largely motivated by application to computational fluid dynamics (CFD). It has utilized the method of lines, where a 3-dimensional spatial domain is discretized to yield a set of coupled ordinary differential

equations in time for the grid values, which are then integrated, e.g. by a Runge-Kutta procedure. This 3 + 1 approach is not applicable to the 2 + 1 + 1 format of characteristic evolution considered here, in which the discretization of a 2-dimensional spherical set of characteristics leads to coupled 2-dimensional partial differential equations in the plane spanned by the outgoing and ingoing characteristics. This 2 + 1 + 1 approach is natural to general relativity since the characteristics (light rays) are fundamental to describing the dynamical geometry of spacetime. It would be impractical in CFD in which the characteristics have a complicated dynamic relation (determined by equations of state) to the fixed Euclidean geometry. As a result, characteristic evolution algorithms were developed only recently in the context of general relativity and there has been relatively little analysis of their computational properties. In particular, for CFD or any symmetric hyperbolic system, numerical dissipation can be added in the standard Kreiss-Oliger form [34]. One of the main results of this paper is to show how analogous dissipation can be successfully applied in a 2 + 1 + 1 format. In the original version of the PITT code, which used square stereographic patches with boundaries aligned with the grid, numerical dissipation was only introduced in the radial direction [35]. This was sufficient to establish numerical stability. In the new version of the code with circular stereographic patches, whose boundaries do not fit regularly on the stereographic grid, numerical dissipation is necessary to control the high frequency error introduced by the intergrid interpolations, as previously noted in the treatment of a fluid problem using circular stereographic patches [28]. We begin with a brief review of the formalism underlying the characteristic evolution code in Sec. II and show how the essential new feature of angular dissipation can be incorporated.

The two spherical grid methods, stereographic and cubed sphere, are briefly described in Sec. IV. We present the test results in Secs. V and VI and we summarize our conclusions in Sec. VII.

II. CHARACTERISTIC FORMALISM

The characteristic formalism is based upon a family of outgoing null hypersurfaces, emanating from some inner worldtube, which extend to infinity where they foliate $\mathcal{I}^+$ into spherical slices. We let u label these hypersurfaces, x^A ($A = 2, 3$) be angular coordinates which label the null rays and r be a surface area coordinate. In the resulting $x^\alpha = (u, r, x^A)$ coordinates, the metric takes the Bondi-Sachs form [1,2]

$$ds^2 = -\left(e^{2\beta}\frac{V}{r} - r^2 h_{AB}U^A U^B\right)du^2 - 2e^{2\beta}dudr - 2r^2 h_{AB}U^B dudx^A + r^2 h_{AB}dx^A dx^B, \quad (2.1)$$

where $h^{AB}h_{BC} = \delta^A_C$ and $\det(h_{AB}) = \det(q_{AB})$, with q_{AB} a unit sphere metric. In analyzing the Einstein equations, we also use the intermediate variable

$$Q_A = r^2 e^{-2\beta} h_{AB} U^B_{,r}. \quad (2.2)$$

The code introduces an auxiliary unit sphere metric q_{AB}, with associated complex dyad q_A satisfying $q_{AB} = \frac{1}{2}\times(q_A\bar{q}_B + \bar{q}_A q_B)$. For a general Bondi-Sachs metric, h_{AB} can then be represented by its dyad component $J = h_{AB}q^A q^B/2$, with the spherically symmetric case characterized by $J = 0$. The full nonlinear h_{AB} is uniquely determined by J, since the determinant condition implies that the remaining dyad component $K = h_{AB}q^A\bar{q}^B/2$ satisfies $1 = K^2 - J\bar{J}$. We also introduce spin-weighted fields $U = U^A q_A$ and $Q = Q_A q^A$, as well as the (complex differential) operators $\eth$ and $\bar{\eth}$ [36]. Refer to [6,30] for further details.

In this formalism, the Einstein equations $G_{\mu\nu} = 0$ decompose into hypersurface equations, evolution equations and conservation conditions on the inner worldtube. As described in more detail in [37,38], the hypersurface equations take the form

$$\beta_{,r} = N_\beta, \quad (2.3)$$

$$U_{,r} = r^{-2}e^{2\beta}Q + N_U, \quad (2.4)$$

$$(r^2 Q)_{,r} = -r^2(\bar{\eth}J + \eth K)_{,r} + 2r^4\eth(r^{-2}\beta)_{,r} + N_Q, \quad (2.5)$$

$$V_{,r} = \frac{1}{2}e^{2\beta}\mathcal{R} - e^\beta\eth\bar{\eth}e^\beta + \frac{1}{4}r^{-2}(r^4(\eth\bar{U} + \bar{\eth}U))_{,r} + N_W, \quad (2.6)$$

where [30]

$$\mathcal{R} = 2K - \eth\bar{\eth}K + \frac{1}{2}(\bar{\eth}^2 J + \eth^2\bar{J}) + \frac{1}{4K}(\bar{\eth}\bar{J}\eth J - \bar{\eth}J\eth\bar{J}) \quad (2.7)$$

is the curvature scalar of the 2-metric h_{AB}. The evolution equation takes the form

$$2(rJ)_{,ur} - (r^{-1}V(rJ)_{,r})_{,r} = -r^{-1}(r^2\eth U)_{,r} + 2r^{-1}e^\beta\eth^2 e^\beta - (r^{-1}V)_{,r}J + N_J, \quad (2.8)$$

where, N_β, N_U, N_Q, N_W, and N_J are nonlinear terms which vanish for spherical symmetry. Expressions for these terms as complex spin-weighted fields and a discussion of the conservation conditions are given in [6].

The characteristic evolution code implements this formalism as an explicit finite difference scheme. In this paper we use second order accurate finite differences and we reduce all angular derivatives to first order by the introduction of auxiliary variables, as described in [39].

A. Angular dissipation

It is a feature of the composite mesh technique that numerical dissipation is necessary to stabilize the error

introduced by intergrid interpolations. In the case of a square stereographic patch, whose boundary aligns with the grid lines, the dissipation built into the characteristic radial integration scheme is sufficient for this purpose [35]. However, because a circular boundary fits into a stereographic grid in an irregular way, angular dissipation is also necessary in order to suppress the resulting high frequency error introduced by the interpolations between stereographic patches.

We accomplish this by modifying the evolution Eq. (2.8) as follows. In the code, (2.8) is expressed in terms of a compactified radial coordinate $x = r/(R + r)$, where R is an adjustable scale parameter and $\mathcal{I}^+$ has finite coordinate value $x = 1$. The evolution in retarded time u is carried out in terms of the variable $\Phi = xJ$, which is regular at $\mathcal{I}^+$. Then the evolution Eq. (2.8) takes the form

$$\partial_u((1-x)\Phi_{,x} + \Phi) = S, \tag{2.9}$$

where S represents the right hand side terms. We add angular dissipation to the u-evolution through the modification

$$\partial_u((1-x)\Phi_{,x} + \Phi) + \epsilon_u h^3 \eth^2 \mathcal{W} \bar{\eth}^2((1-x)\Phi_{,x} + \Phi) = S, \tag{2.10}$$

where h is the discretization size, $\epsilon_u \geq 0$ is an adjustable parameter independent of h and $\mathcal{W}$ is a positive weighting function with $\mathcal{W} = 1$ inside the equator and $\mathcal{W} = 0$ at the patch boundary. This leads to

$$\begin{aligned}\partial_u(|(1-x)\Phi_{,x} + \Phi|^2) + 2\epsilon_u h^3 \Re\{&((1-x)\bar{\Phi}_{,x} \\ &+ \bar{\Phi})\eth^2 \mathcal{W} \bar{\eth}^2((1-x)\Phi_{,x} + \Phi)\} \\ &= 2\Re\{((1-x)\bar{\Phi}_{,x} + \bar{\Phi})S\}.\end{aligned} \tag{2.11}$$

Integration over the unit sphere with solid angle element $d\Omega$ then gives

$$\begin{aligned}\partial_u \oint |(1-x)\Phi_{,x} + \Phi|^2 d\Omega + 2\epsilon_u h^3 \oint \mathcal{W} \\ \times |\bar{\eth}^2((1-x)\Phi_{,x} + \Phi)|^2 d\Omega \\ = 2\Re \oint ((1-x)\bar{\Phi}_{,x} + \bar{\Phi}) S d\Omega.\end{aligned} \tag{2.12}$$

Thus the ϵ_u-term has the effect of damping high frequency noise as measured by the L_2 norm of $(1-x)\Phi_{,x} + \Phi$ over the sphere.

Similarly, dissipation is introduced in the radial integration of (2.9) through the substitution

$$\begin{aligned}\partial_u((1-x)\Phi_{,x} + \Phi) \rightarrow \partial_u((1-x)\Phi_{,x} + \Phi) \\ + \epsilon_x h^3 \eth^2 \mathcal{W} \bar{\eth}^2 \Phi_{,u}\end{aligned} \tag{2.13}$$

with $\epsilon_x \geq 0$. Angular dissipation is also introduced in the hypersurface equations through the substitutions

$$(r^2 Q)_{,r} \rightarrow (r^2 Q)_{,r} + \epsilon_Q h^3 \eth\bar{\eth} \mathcal{W} \eth\bar{\eth} r Q \tag{2.14}$$

$$V_{,r} \rightarrow V_{,r} + \epsilon_V h^3 \eth\bar{\eth} \mathcal{W} \eth\bar{\eth} V. \tag{2.15}$$

III. WAVEFORMS AT $\mathcal{I}^+$

For an analytic treatment of the Penrose compactification of an asymptotically flat spacetime, it is simplest to introduce an inverse radial coordinate $\ell = 1/r$, so that future null infinity $\mathcal{I}^+$ is given by $\ell = 0$ [40]. In the resulting $x^\mu = (u, \ell, x^A)$ conformal Bondi coordinates, the physical spacetime metric $g_{\mu\nu}$ has the conformal compactification $\hat{g}_{\mu\nu} = \ell^2 g_{\mu\nu}$, where $\hat{g}_{\mu\nu}$ is smooth at $\mathcal{I}^+$ and, referring to (2.1), takes the form

$$\begin{aligned}\hat{g}_{\mu\nu} dx^\mu dx^\nu = &-(e^{2\beta} V \ell^3 - h_{AB} U^A U^B) du^2 + 2e^{2\beta} du d\ell \\ &- 2h_{AB} U^B du dx^A + h_{AB} dx^A dx^B.\end{aligned} \tag{3.1}$$

The inverse conformal metric has the non vanishing components $\hat{g}^{u\ell} = e^{-2\beta}$, $\hat{g}^{\ell\ell} = e^{-2\beta}\ell^3 V$, $\hat{g}^{\ell A} = e^{-2\beta} U^A$ and $\hat{g}^{AB} = h^{AB}$.

The Bondi mass, news function and Ψ_4^0 (functions of u and x^A), which describe the total energy and radiation power, are constructed from the leading coefficients in an expansion of the metric in powers of ℓ. The requirement of an asymptotically flat vacuum exterior imposes relations between these expansion coefficients. In the $\hat{g}_{\mu\nu}$ conformal frame, the vacuum gravitational equations are

$$-\ell^2 \hat{G}_{\mu\nu} = 2\ell(\hat{\nabla}_\mu \hat{\nabla}_\nu \ell - \hat{g}_{\mu\nu} \hat{\nabla}^\alpha \hat{\nabla}_\alpha \ell) + 3\hat{g}_{\mu\nu}(\hat{\nabla}^\alpha \ell)\hat{\nabla}_\alpha \ell \tag{3.2}$$

in terms of the Einstein tensor $\hat{G}_{\mu\nu}$ and covariant derivative $\hat{\nabla}_\mu$ associated with $\hat{g}_{\mu\nu}$. Asymptotic flatness immediately implies that $\hat{g}^{\ell\ell} = (\hat{\nabla}^\alpha \ell)\hat{\nabla}_\alpha \ell = O(\ell)$ so that $\mathcal{I}^+$ is null. From the trace of (3.2), we have

$$(\hat{\nabla}^\alpha \ell)\hat{\nabla}_\alpha \ell = \frac{1}{2}\ell\hat{\Theta} + O(\ell^2), \tag{3.3}$$

where

$$\hat{\Theta} := \hat{\nabla}^\mu \hat{\nabla}_\mu \ell = e^{-2\beta}(\partial_\ell(\ell^3 V) + \partial_A U^A) \tag{3.4}$$

is smooth at $\mathcal{I}^+$. In addition, (3.2) implies the existence of a smooth trace-free field $\hat{\Sigma}_{\mu\nu}$ defined by

$$\ell\hat{\Sigma}_{\mu\nu} := \hat{\nabla}_\mu \hat{\nabla}_\nu \ell - \frac{1}{4}\hat{g}_{\mu\nu}\hat{\Theta}. \tag{3.5}$$

For future reference we introduce an orthonormal null tetrad $(\hat{n}^\mu, \hat{\ell}^\mu, \hat{m}^\mu)$ be such that $\hat{n}^\mu = \hat{\nabla}^\mu \ell$ and $\hat{\ell}^\mu \partial\mu = \partial_\ell$ at $\mathcal{I}^+$. Note that (3.2), (3.4), and (3.5) imply

$$\hat{m}^\nu \hat{m}^\rho \left(\hat{\Sigma}_{\nu\rho} + \frac{1}{2}\hat{G}_{\nu\rho}\right) = 0. \tag{3.6}$$

The gravitational waveform depends on the value of $\hat{\Sigma}_{\mu\nu}$ on $\mathcal{I}^+$, which in turn depends on the leading terms up to $O(\ell)$ in the expansion of $\hat{g}_{\mu\nu}$. We thus expand

$$h_{AB}(u,\ell,x^C) = H_{AB}(u,x^C) + \ell c_{AB}(u,x^C) + O(\ell^2). \tag{3.7}$$

Further conditions on the asymptotic expansion of the metric can be extracted from (3.2). We have

$$\beta(u,\ell,x^C) = H(u,x^C) + O(\ell^2) \tag{3.8}$$

(where the $O(\ell)$ term vanishes),

$$U^A = L^A + 2\ell e^{2H} H^{AB} D_B H + O(\ell^2), \tag{3.9}$$

and

$$\ell^2 V = D_A L^A + \ell(e^{2H}\mathcal{R}/2 + D_A D^A e^{2H}) + O(\ell^2), \tag{3.10}$$

where $\mathcal{R}$ and D_A are the 2-dimensional curvature scalar and covariant derivative associated with h_{AB}. These results combine with (3.4) to give

$$\hat{\Theta} = 2e^{-2H} D_A L^A + \ell(\mathcal{R} + 3e^{-2H} D_A D^A e^{2H}) + O(\ell^2). \tag{3.11}$$

In addition, the requirement that

$$\ell\left(\hat{\Sigma}_{AB} - \frac{1}{2} H_{AB} H^{CD} \Sigma_{CD}\right)$$

vanishes at $\mathcal{I}^+$ implies via (3.5) that

$$2H_{C(A} D_{B)} L^C + \partial_u H_{AB} - H_{AB} D_C L^C = O(\ell). \tag{3.12}$$

The expansion coefficients H, H_{AB}, c_{AB}, and L^A (all functions of (u, x^A)) completely determine the radiation field. One can further specialize the Bondi coordinates to be *inertial* at $\mathcal{I}^+$, i.e. have Minkowski form, in which case $H = L^A = 0$, $H_{AB} = q_{AB}$ (the unit sphere metric) so that (3.12) is trivially satisfied and the radiation field is determined by c_{AB}. However, the characteristic extraction of the waveform is carried out in null coordinates determined by data on the inner worldtube so that this *inertial* simplification cannot be assumed.

A. Calculation of the news

The following calculation of the Bondi news streamlines the presentation in [5] and corrects errors. In order to carry out the calculation in the $\hat{g}_{\mu\nu}$ computational frame, it is useful to refer to an inertial conformal Bondi frame [40] with metric $\tilde{g}_{\mu\nu} = \Omega^2 g_{\mu\nu} = \omega^2 \hat{g}_{\mu\nu}$, where $\Omega = \omega\ell$, which satisfies the gauge requirements that $Q_{AB} := \tilde{g}_{AB}|_{\mathcal{I}^+} = \omega^2 H_{AB}$ is intrinsically a unit sphere metric at $\mathcal{I}^+$ and that $(\tilde{\nabla}^\alpha \Omega)\tilde{\nabla}_\alpha \Omega = O(\Omega^2)$. (See [41] for a discussion of how the news in an arbitrary conformal frame is related to its expression in this inertial Bondi frame.)

$\mathcal{I}^+$ is a null hypersurface with the null vector $\tilde{n}^\alpha = \tilde{g}^{\alpha\beta}\nabla_\beta \Omega|_{\mathcal{I}^+}$, or equivalently, $\hat{n}^\alpha = \hat{g}^{\alpha\beta}\nabla_\beta \ell|_{\mathcal{I}^+} = \omega\tilde{n}^\alpha$, tangent to its generators. In order to complete a basis for tangent vectors to $\mathcal{I}^+$, let $\mathcal{Q}^\alpha$ be a complex field tangent to $\mathcal{I}^+$ satisfying $\mathcal{Q}^\alpha \tilde{n}_\alpha = 0$, $\tilde{g}_{\alpha\beta}\mathcal{Q}^\alpha \mathcal{Q}^\beta|_{\mathcal{I}^+} = 0$, and $\tilde{g}_{\alpha\beta}\mathcal{Q}^\alpha \bar{\mathcal{Q}}^\beta|_{\mathcal{I}^+} = 2$. In an inertial conformal Bondi frame, the news function can then be expressed as [5]

$$N = \lim_{\Omega\to 0} \frac{1}{2\Omega} \mathcal{Q}^\alpha \mathcal{Q}^\beta \tilde{\nabla}_\alpha \tilde{\nabla}_\beta \Omega \tag{3.13}$$

evaluated in the limit of $\mathcal{I}^+$. (Our conventions are chosen so that the news reduces to Bondi's original expression in the axisymmetric case [1]). In terms of the $\hat{g}_{\alpha\beta}$ frame, with conformal factor $\ell = \Omega/\omega$, we then have

$$N = \lim_{\ell\to 0} \frac{1}{2} \mathcal{Q}^\alpha \mathcal{Q}^\beta \left(\frac{\hat{\nabla}_\alpha \hat{\nabla}_\beta \ell}{\ell} - \omega \hat{\nabla}_\alpha \hat{\nabla}_\beta \frac{1}{\omega} + \frac{1}{\ell\omega} \hat{g}_{\alpha\beta} (\hat{\nabla}^\mu \ell) \hat{\nabla}_\mu \omega \right) \tag{3.14}$$

$$= \frac{1}{2} \mathcal{Q}^\alpha \mathcal{Q}^\beta \left(\hat{\Sigma}_{\alpha\beta} - \omega \hat{\nabla}_\alpha \hat{\nabla}_\beta \frac{1}{\omega} + \frac{1}{\omega} (\partial_\ell \hat{g}_{\alpha\beta}) \times (\hat{\nabla}^\mu \ell) \hat{\nabla}_\mu \omega \right). \tag{3.15}$$

[This corrects an error in Eq. (30) of [5].] We determine ω on $\mathcal{I}^+$ in the $\hat{g}_{\alpha\beta}$ frame by solving the elliptic equation governing the conformal transformation of the curvature scalar (2.7) of the geometry intrinsic to a $u =$ constant cross section to a unit sphere geometry,

$$\mathcal{R} = 2(\omega^2 + H^{AB} D_A D_B \log\omega). \tag{3.16}$$

The condition that $(\tilde{\nabla}^\alpha \Omega)\tilde{\nabla}_\alpha \Omega = O(\Omega^2)$ determines the time dependence of ω,

$$2\hat{n}^\alpha \partial_\alpha \log\omega = -e^{-2H} D_A L^A, \tag{3.17}$$

which is used to evolve ω given a solution of (3.16) as initial condition.

In order to obtain an explicit expression for the news (3.15) in the $\hat{g}_{\alpha\beta}$ frame we need to fix the choice of $\mathcal{Q}^\beta$. The freedom $\mathcal{Q}^\beta \to \mathcal{Q}^\beta + \lambda\tilde{n}^\beta$ leaves (3.15) invariant but it is important for physical interpretation to choose the spin rotation freedom $\mathcal{Q}^\beta \to e^{-i\alpha}\mathcal{Q}^\beta$ to satisfy $\tilde{n}^\alpha \tilde{\nabla}_\alpha \mathcal{Q}^\beta = O(\Omega)$, so that the polarization frame is parallel propagated along the generators of $\mathcal{I}^+$. This fixes the polarization modes determined by the real and imaginary parts of the news to correspond to those of inertial observers at $\mathcal{I}^+$.

We accomplish this by introducing the dyad decomposition $H^{AB} = (F^A \bar{F}^B + \bar{F}^A F^B)/2$ where

$$F^A = q^A \sqrt{\frac{(K+1)}{2}} - \bar{q}^A J \sqrt{\frac{1}{2(K+1)}}. \tag{3.18}$$

We set $\mathcal{Q}^\beta = e^{-i\delta}\omega^{-1} F^\beta + \lambda\tilde{n}^\beta$, where $F^\alpha := (0, 0, F^A)$. The requirement of an inertial polarization frame, $\tilde{n}^\alpha \tilde{\nabla}_\alpha \mathcal{Q}^\beta = O(\Omega)$, then determines the time dependence of the phase δ. We obtain, after using (3.17) to eliminate the time derivative of ω,

$$2i(\partial_u + L^A\partial_A)\delta = D_A L^A + H_{AC}\bar{F}^C((\partial_u + L^B\partial_B)F^A - F^B\partial_B L^A). \tag{3.19}$$

We can now express the inertial news (3.15) in the $\hat{g}_{\alpha\beta}$ frame as

$$N = \frac{1}{2}e^{-2i\delta}\omega^{-2}F^\alpha F^\beta\Big(\hat{\Sigma}_{\alpha\beta} - \omega\hat{\nabla}_\alpha\hat{\nabla}_\beta\frac{1}{\omega} + \frac{1}{\omega}(\partial_\ell\hat{g}_{\alpha\beta}) \times (\hat{\nabla}^\mu\ell)\hat{\nabla}_\mu\omega\Big). \tag{3.20}$$

with $F^\alpha = (0, 0, F^A)$. An explicit calculation leads to

$$N = \frac{1}{4}e^{-2i\delta}\omega^{-2}e^{-2H}F^A F^B\{(\partial_u + \mathcal{L}_L)c_{AB} - \frac{1}{2}c_{AB}D_C L^C + 2\omega D_A[\omega^{-2}D_B(\omega e^{2H})]\}, \tag{3.21}$$

where $\mathcal{L}_L$ denotes the Lie derivative with respect to L^A. This corrects a minus sign error in Eq. (38) of [5], where spin-weighted expressions for the terms in (3.21) are given.

In inertial Bondi coordinates, the expression for the news function reduces to the simple form

$$N = \frac{1}{4}Q^A Q^B\partial_u c_{AB}. \tag{3.22}$$

However, the general form (3.21) must be used in the computational coordinates, which is challenging for maintaining accuracy because of the appearance of second angular derivatives of ω.

B. Calculation of the Weyl tensor

Asymptotic flatness implies that the Weyl tensor vanishes at $\mathcal{I}^+$, i.e. $\hat{C}_{\mu\nu\rho\sigma} = O(\ell)$ in the $\hat{g}_{\mu\nu}$ conformal Bondi frame (3.1). This is the conformal space version of the peeling property of asymptotically flat spacetimes [3]. In terms of the orthonormal null tetrad $(\hat{n}^\mu, \hat{\ell}^\mu, \hat{m}^\mu)$, with $\hat{n}^\mu = \hat{\nabla}^\mu\ell$ and $\hat{\ell}^\mu\partial\mu = \partial_\ell$ at $\mathcal{I}^+$, the radiation is described by the limit

$$\hat{\Psi} := -\frac{1}{2}\lim_{\ell\to 0}\frac{1}{\ell}\hat{n}^\mu\hat{m}^\nu\hat{n}^\rho\hat{m}^\sigma\hat{C}_{\mu\nu\rho\sigma}, \tag{3.23}$$

which corresponds in Newman-Penrose notation to $-(1/2)\bar{\psi}^0_4$. The limit is independent of how the tetrad is extended off $\mathcal{I}^+$ but to simplify the calculation we make the following choices adapted to our conformal Bondi coordinates. We set $\hat{\ell}^\mu = e^{2\beta}\hat{\nabla}^\mu u$, $\hat{n}^\mu = \hat{\nabla}^\mu\ell + O(\ell)$, $\hat{\ell}^\rho\hat{\nabla}_\rho\hat{m}^\mu = 0$ and $\hat{\ell}^\rho\hat{\nabla}_\rho\hat{n}^\mu = 0$, which implies

$$\hat{n}_\mu = \hat{\nabla}_\mu\ell - \frac{\ell}{4}\hat{\ell}_\mu\hat{\Theta} + O(\ell^2). \tag{3.24}$$

Our main calculational result is

$$\hat{\Psi} = \frac{1}{2}\hat{n}^\mu\hat{m}^\nu\hat{m}^\rho(\hat{\nabla}_\mu\hat{\Sigma}_{\nu\rho} - \hat{\nabla}_\nu\hat{\Sigma}_{\mu\rho})|_{\mathcal{I}^+}, \tag{3.25}$$

and that (3.25) is independent of the freedom

$$\hat{m}^\nu \to \hat{m}^\nu + \lambda\hat{n}^\nu. \tag{3.26}$$

The result (3.25) follows from the following sequence of calculations beginning with (3.23) (where evaluation at $\mathcal{I}^+$ is assumed)

$$-2\hat{\Psi} = \frac{1}{\ell}\hat{n}^\mu\hat{m}^\nu\hat{n}^\rho\hat{m}^\sigma\hat{C}_{\mu\nu\rho\sigma} \tag{3.27}$$

$$= \frac{1}{\ell}\hat{n}^\mu\hat{m}^\nu\hat{n}^\rho\hat{m}^\sigma\hat{R}_{\mu\nu\rho\sigma} \tag{3.28}$$

$$= -\frac{1}{\ell}\hat{n}^\mu\hat{m}^\nu\hat{m}^\rho(\hat{\nabla}_\mu\hat{\nabla}_\nu\hat{n}_\rho - \hat{\nabla}_\nu\hat{\nabla}_\mu\hat{n}_\rho) \tag{3.29}$$

$$= -\frac{1}{\ell}\hat{n}^\mu\hat{m}^\nu\hat{m}^\rho\Big(\hat{\nabla}_\mu(\ell\hat{\Sigma}_{\nu\rho}) - \hat{\nabla}_\nu(\ell\hat{\Sigma}_{\mu\rho}) - \hat{\nabla}_\mu\hat{\nabla}_\nu\Big(\frac{\ell\hat{\Theta}}{4}\ell_\rho\Big) + \hat{\nabla}_\nu\hat{\nabla}_\mu\Big(\frac{\ell\hat{\Theta}}{4}\ell_\rho\Big)\Big) \tag{3.30}$$

$$= -\hat{n}^\mu\hat{m}^\nu\hat{m}^\rho(\hat{\nabla}_\mu\hat{\Sigma}_{\nu\rho} - \hat{\nabla}_\nu\hat{\Sigma}_{\mu\rho}) - \frac{1}{\ell}\hat{n}^\mu\hat{m}^\nu\hat{m}^\rho\Big(\hat{\Sigma}_{\nu\rho}\hat{\nabla}_\mu\ell - \hat{\Sigma}_{\mu\rho}\hat{\nabla}_\nu\ell - \hat{\nabla}_\mu\hat{\nabla}_\nu\Big(\frac{\ell\hat{\Theta}}{4}\ell_\rho\Big) + \hat{\nabla}_\nu\hat{\nabla}_\mu\Big(\frac{\ell\hat{\Theta}}{4}\ell_\rho\Big)\Big) \tag{3.31}$$

$$= -\hat{n}^\mu\hat{m}^\nu\hat{m}^\rho(\hat{\nabla}_\mu\hat{\Sigma}_{\nu\rho} - \hat{\nabla}_\nu\hat{\Sigma}_{\mu\rho}) - \frac{1}{\ell}\hat{n}^\mu\hat{m}^\nu\hat{m}^\rho\Big(\hat{\Sigma}_{\nu\rho}\frac{\ell\hat{\Theta}}{4}\ell_\mu - \hat{\Sigma}_{\mu\rho}\frac{\ell\hat{\Theta}}{4}\ell_\nu - \hat{\nabla}_\mu\hat{\nabla}_\nu\Big(\frac{\ell\hat{\Theta}}{4}\ell_\rho\Big) + \hat{\nabla}_\nu\hat{\nabla}_\mu\Big(\frac{\ell\hat{\Theta}}{4}\ell_\rho\Big)\Big) \tag{3.32}$$

$$= -\hat{n}^\mu\hat{m}^\nu\hat{m}^\rho(\hat{\nabla}_\mu\hat{\Sigma}_{\nu\rho} - \hat{\nabla}_\nu\hat{\Sigma}_{\mu\rho}) - \frac{\hat{\Theta}}{4}\hat{m}^\nu\hat{m}^\rho(\hat{\Sigma}_{\nu\rho} - n^\mu\ell^\sigma\hat{R}_{\mu\nu\rho\sigma}) \tag{3.33}$$

$$= -\hat{n}^\mu\hat{m}^\nu\hat{m}^\rho(\hat{\nabla}_\mu\hat{\Sigma}_{\nu\rho} - \hat{\nabla}_\nu\hat{\Sigma}_{\mu\rho}) - \frac{\hat{\Theta}}{4}\hat{m}^\nu\hat{m}^\rho \times (\hat{\Sigma}_{\nu\rho} - \hat{n}^\mu\ell^\sigma(\hat{g}_{\mu[\nu}\hat{G}_{\sigma]\rho} - \hat{g}_{\rho[\nu}\hat{G}_{\sigma]\mu})) \tag{3.34}$$

$$= -\hat{n}^\mu\hat{m}^\nu\hat{m}^\rho(\hat{\nabla}_\mu\hat{\Sigma}_{\nu\rho} - \hat{\nabla}_\nu\hat{\Sigma}_{\mu\rho}) - \frac{\hat{\Theta}}{4}\hat{m}^\nu\hat{m}^\rho\Big(\hat{\Sigma}_{\nu\rho} + \frac{1}{2}\hat{G}_{\nu\rho}\Big) \tag{3.35}$$

$$= -\hat{n}^\mu\hat{m}^\nu\hat{m}^\rho(\hat{\nabla}_\mu\hat{\Sigma}_{\nu\rho} - \hat{\nabla}_\nu\hat{\Sigma}_{\mu\rho}). \tag{3.36}$$

Here (3.28) follows because all trace terms vanish; (3.29) follows from the commutator of covariant derivatives; (3.30) follows from (3.5); (3.31) follows from differentiation; (3.32) follows from (3.24); (3.33) follows from taking leading terms and using the covariant commutator; (3.34)

follows from the vanishing of the Weyl tensor at $\mathcal{I}^+$; (3.35) follows algebraically; and (3.36) follows from (3.6).

Invariance of $\hat{\Psi}$ under the freedom (3.26) follows from noting that

$$\hat{n}^\mu \hat{m}^\nu \hat{n}^\rho \hat{n}^\sigma \hat{C}_{\mu\nu\rho\sigma} = 0 \tag{3.37}$$

and then following the steps analogous to (3.27), (3.28), (3.29), (3.30), (3.31), (3.32), (3.33), (3.34), (3.35), and (3.36) to show

$$\hat{n}^\mu \hat{m}^\nu \hat{n}^\rho (\hat{\nabla}_\mu \hat{\Sigma}_{\nu\rho} - \hat{\nabla}_\nu \hat{\Sigma}_{\mu\rho})|_{\mathcal{I}^+} = 0. \tag{3.38}$$

Finally, the Weyl tensor must be scaled intrinsic to the $\tilde{g}_{\mu\nu}$ conformal frame in order to describe the radiation observed by inertial observers at $\mathcal{I}^+$. The conformal transformation $\tilde{g}_{\mu\nu} = \omega^2 \hat{g}_{\mu\nu}$ gives for the inertial radiation field

$$\begin{aligned}\Psi &:= -\frac{1}{2}\lim_{\Omega\to 0}\frac{1}{\Omega}\tilde{n}^\mu \mathcal{Q}^\nu \tilde{n}^\rho \mathcal{Q}^\sigma \tilde{C}_{\mu\nu\rho\sigma} \\ &= -\frac{1}{2}\omega^{-3} e^{-2i\delta}\lim_{\ell\to 0}\frac{1}{\ell}\hat{n}^\mu F^\nu \hat{n}^\rho F^\sigma \hat{C}_{\mu\nu\rho\sigma},\end{aligned} \tag{3.39}$$

where $\mathcal{Q}^\beta = e^{-i\delta}\omega^{-1}F^\beta + \lambda\tilde{n}^\beta$ is the same inertial polarization dyad used in describing the news (3.21). From (3.25), we then have

$$\Psi = \frac{1}{2}\omega^{-3} e^{-2i\delta}\hat{n}^\mu F^\nu F^\rho (\hat{\nabla}_\mu \hat{\Sigma}_{\nu\rho} - \hat{\nabla}_\nu \hat{\Sigma}_{\mu\rho})|_{\mathcal{I}^+}. \tag{3.40}$$

We next need to express Ψ in terms of the computational variables. The straightforward way is to expand (3.40) as

$$\begin{aligned}\Psi = \frac{1}{2}\omega^{-3} e^{-2i\delta}\hat{n}^\mu F^A F^B (&\partial_\mu \hat{\Sigma}_{AB} - \partial_A \hat{\Sigma}_{\mu B} \\ &- \hat{\Gamma}^\alpha_{\mu B}\hat{\Sigma}_{A\alpha} + \hat{\Gamma}^\alpha_{AB}\hat{\Sigma}_{\mu\alpha})|_{\mathcal{I}^+}.\end{aligned} \tag{3.41}$$

and calculate the individual components of $\hat{\Sigma}_{\mu\nu}$ in terms of those variables. This involves lengthy algebra, which is simplified by the following intermediate results which hold at $\mathcal{I}^+$:

$$\hat{\Sigma}_{\ell\ell} = -2\partial_\ell^2 \beta \tag{3.42}$$

$$\hat{\Sigma}_{\ell A} = \frac{1}{2}e^{-2H}\partial_\ell (h_{AB}\partial_\ell U^B) \tag{3.43}$$

$$\hat{\Sigma}_{\ell u} = \frac{1}{4}e^{2H}\mathcal{R} + \frac{1}{4}D_A D^A e^{2H} - L^A \hat{\Sigma}_{\ell A} \tag{3.44}$$

$$(\hat{\nabla}^\mu \ell)(\hat{\nabla}^\nu \ell)\hat{\Sigma}_{\mu\nu} = \frac{1}{2}e^{-2H}(\partial_u + L^A\partial_A)(e^{-2H}D_A L^A) \tag{3.45}$$

$$(\hat{\nabla}^\mu \ell)\hat{\Sigma}_{\mu A} = \frac{1}{2}\partial_A (e^{-2H}D_B L^B) \tag{3.46}$$

$$\begin{aligned}\hat{\Sigma}_{AB} = &\frac{1}{2}e^{-2H}(\partial_u + \mathcal{L}_L)c_{AB} + e^{-2H}D_A D_B e^{2H} \\ &- \frac{1}{4}H_{AB}(\mathcal{R} + 3e^{-2H}D^C D_C e^{2H}).\end{aligned} \tag{3.47}$$

We use a Maple script to convert these expressions in terms of ð operators acting on the spin-weighted computational fields and construct the final Fortran expression for Ψ.

In inertial Bondi coordinates, (3.41) reduces to

$$\Psi = \frac{1}{4}Q^A Q^B \partial_u^2 c_{AB} = \partial_u^2 \partial_l J|_{\mathcal{I}}^+. \tag{3.48}$$

This is related to the expression for the news function in inertial Bondi coordinates by

$$\Psi = \partial_u N. \tag{3.49}$$

However, as in the case of the news, the full expression (3.41) for Ψ must be used in the code. This introduces additional challenges to numerical accuracy due to the large number of terms and the appearance of third angular derivatives.

C. Linearized expressions

The general nonlinear representation of Ψ in (3.41) in terms of the computational variables is quite long but reduces to a simpler form in the linearized approximation, i.e. to first order in perturbations off a Minkowski background. In terms of the spin-weighted fields $J = h_{AB}q^A Q^B/2$ and $L = L^A q_A$, we find

$$\Psi = -\frac{1}{2}\hat{\Sigma}_{\ell u}\eth L + \partial_u \hat{\Sigma}_J - \frac{1}{2}\eth \hat{\Sigma}_u - \frac{1}{2}\partial_u J(\hat{\Sigma}_{\ell u} + \hat{\Sigma}_K) \tag{3.50}$$

(evaluated at $\mathcal{I}^+$), where the only nonvanishing zeroth order parts of $\hat{\Sigma}_{\mu\nu}$ are

$$\hat{\Sigma}_K \equiv \frac{1}{2}q^A \bar{q}^B \hat{\Sigma}_{AB} = -\frac{1}{2}, \qquad \hat{\Sigma}_{\ell u} = \frac{1}{2} \tag{3.51}$$

and the required first order components are

$$\hat{\Sigma}_J \equiv \frac{1}{2}q^A q^B \hat{\Sigma}_{AB} = \eth^2 H - \frac{1}{2}J + \frac{1}{2}\partial_u \partial_\ell J \tag{3.52}$$

$$\hat{\Sigma}_u \equiv q^A \hat{\Sigma}_{uA} = \frac{1}{4}\eth^2 \bar{L} + \frac{1}{4}\eth\bar{\eth}L + \frac{1}{2}L. \tag{3.53}$$

Then (3.50) reduces to

$$\Psi = \frac{1}{2}\partial_u^2 \partial_\ell J - \frac{1}{2}\partial_u J - \frac{1}{2}\eth L - \frac{1}{8}\eth^2(\eth\bar{L} + \bar{\eth}L) + \partial_u \eth^2 H. \tag{3.54}$$

In the same approximation, the news function is given by

$$N = \frac{1}{4} q^A q^B (\partial_u c_{AB} + 2 D_A D_B (\omega + 2H)) = \frac{1}{2} \partial_u \partial_\ell J + \frac{1}{2} \eth^2 (\omega + 2H). \quad (3.55)$$

Using the asymptotic relations

$$\partial_u J = -\eth L \quad (3.56)$$

$$\partial_u \omega = -\frac{1}{4} (\eth \bar{L} + \bar{\eth} L), \quad (3.57)$$

which arise from the linearized versions of (3.12) and (3.17), it is easy to see that (3.49), i.e. $\Psi = \partial_u N$, still holds in the linearized approximation. (In the nonlinear case, the derivative along the generators of $\mathcal{I}^+$ is $\hat{n}^\mu \partial_\mu = e^{-2H}(\partial_u + L^A \partial_A)$ and (3.49) must be modified accordingly.)

The linearized expressions (3.54) and (3.55) provide a starting point to compare the advantages between computing the radiation via the Weyl component Ψ or the news function N. The troublesome terms involve L, H and ω, which all vanish in inertial Bondi coordinates. One main difference is that Ψ contains third order angular derivatives, e.g. $\eth^3 \bar{L}$, as opposed to second angular derivatives for N. This means that the smoothness of the numerical error is more crucial in the Ψ approach. Balancing this, another main difference is that N contains the $\eth^2 \omega$ term, which is a potential source of numerical error since ω must be propagated across patch boundaries via (3.17).

D. Summary of the gravitational radiation calculation

The characteristic Einstein equations are evolved in a domain between an inner radial boundary at the interior worldtube, and an outer boundary at future null infinity. Initial data for $J(u, r, x^A)$ is required at $u = 0$. This data is constraint-free so that, in the absence of an exact solution or other prescription of the data, we can simply set $J(0, r, x^A) = 0$. Alternatively, in order to reduce spurious initial radiation, we can set the Newman-Penrose Weyl tensor component $\Psi_0(0, r, x^A) = 0$, which determines $J(0, r, x^A)$ when continuity conditions are imposed at the inner worldtube. The metric data from a Cauchy evolution is interpolated onto the inner worldtube to extract the boundary data for the characteristic evolution. This extraction process involves carrying out the complicated Jacobian transformation between the Cartesian coordinates used in the Cauchy evolution and the spherical null coordinates used in the characteristic evolution. The full details are given in [10]. The result is boundary data for J, β, U, Q, V on the worldtube, which supply the integration constants for a radial numerical integration of (2.3), (2.4), (2.5), and (2.6), in that order. Given the initial data $J(0, r, x^A)$, this leads to complete knowledge of the metric on the initial null cone. Then (2.8) gives an expression for $J_{,ur}$, which is used to determine J on the "next" null cone, so that the process can be repeated to yield the complete metric throughout the domain, which extends to $\mathcal{I}^+$.

Before the gravitational radiation is calculated from the metric in the neighborhood of $\mathcal{I}^+$, it is necessary to compute the auxiliary variables $\omega(u, x^A)$ and $\delta(u, x^A)$ which determine the inertial polarization dyad in which to measure the news function N or Weyl component Ψ. Given a solution of (3.16) for the initial value of $\omega(0, x^A)$, its evolution is computed by integrating (3.17). (If $J = 0$ initially, then $\omega = 1$ is the solution to (3.16). Otherwise, ω is initiated by solving a 2-dimensional elliptic equation.) Similarly, fixing the initial polarization basis by $\delta(0, x^A) = 0$, its evolution is computed by integrating (3.19). Then the news N is given by (3.21) (or in spin-weighted form by the formulas in Appendix B of Ref. [5]) and Ψ is given by (3.41).

The above procedure computes N or Ψ as functions of the code coordinates (u, x^A), rather than inertial coordinates. In the linearized case, which is used for the tests in Sec. VI, the change to inertial coordinates is a second-order effect that can be neglected. However, that is not the case in general and the full procedure is described in Sec. IV B of Ref. [5].

IV. PATCHING THE SPHERE

The nonsingular description of smooth tensor fields on the sphere requires more than a single coordinate patch. Here we consider the stereographic treatment which uses 2 coordinate patches, and the cubed-sphere treatment, which uses 6 patches. In both cases the metric q_{AB} of the unit sphere is expressed in terms of a complex dyad q_A (satisfying $q^A q_A = 0$, $q^A \bar{q}_A = 2$, $q^A = q^{AB} q_B$, with $q^{AB} q_{BC} = \delta^A_C$ and $q_{AB} = \frac{1}{2}(q_A \bar{q}_B + \bar{q}_A q_B)$). The dyads for each patch are related by spin transformations at points common to more than one patch.

A. Circular stereographic patches

In stereographic coordinates, the sphere is covered with two patches, one for each hemisphere. The North hemisphere is covered by the complex stereographic coordinate $\xi_N = \eta_N + i\rho_N$, which is related to standard (θ, ϕ) angular coordinates by $\xi_N = \tan(\theta/2) e^{i\phi}$ and which is regular on the entire sphere except for the South pole. The South hemisphere is covered by the complex stereographic coordinate $\xi_S = 1/\xi_N = \eta_S + i\rho_S = \cot(\theta/2) e^{-i\phi}$, which is singular at the North pole. Every point on the sphere is covered by at least one of the patches, and there is a region around the equator where points are covered by both patches. In this overlap region between the two patches, a scalar function F with value $F_N(\xi_N)$ on the North patch has the value $F_S(\xi_S = 1/\xi_N)$ on the South patch. For a function F of spin-weight s, $F_S(\xi_S = 1/\xi_N) = F_N(\xi_N) \times (-1)^s e^{-2is\Phi}$.

In the $x^A = (\eta, \rho)$ coordinates, the unit sphere metric in each patch is given by

$$q_{AB}dx^A dx^B = \frac{4}{P^2}(d\eta^2 + d\rho^2), \tag{4.1}$$

where

$$P = 1 + \eta^2 + \rho^2. \tag{4.2}$$

The equator corresponds to the circle

$$\sqrt{\eta^2 + \rho^2} = 1. \tag{4.3}$$

We fix the dyad by the explicit choice

$$q^A = \frac{P}{2}(1, i), \qquad i = \sqrt{-1}. \tag{4.4}$$

In the composite mesh method, all boundary points of one patch are interior points of another patch. The overlapping of the patches is key to the stability of this method. The two stereographic coordinate patches must both extend beyond the equator. In the scheme originally used to implement the computational ð-formalism [30] in the characteristic code, the North and South patches were represented by square (η, ρ) grids. In the scheme implemented for meteorological studies [28], circular masks are applied so that the computational grids extend only a few zones beyond the equator. Here we adopt this circular grid boundary but place it a fixed geometrical distance past the equator, i.e. the grid boundary for the North patch is a circle lying in the South patch. The finite buffer zone between the equator and the grid boundary allows for angular dissipation, as developed in Sec. , to damp the high frequency intergrid interpolation error before it crosses the equator. This protects measurements of the news function (or Ψ) in the North patch, which involve two (or three) angular derivatives, from substantial contamination by the interpolation error at the patch boundary.

We discretize the stereographic coordinates according to

$$\begin{aligned} \eta_i &= -1 + (i - O - 1)\Delta, \\ \rho_j &= -1 + (j - O - 1)\Delta \end{aligned} \tag{4.5}$$

where, following the notation in [28], O is the number of points (overlapping points) by which each grid extends beyond the equator and the indices range over $1 \le i, j \le M + 1 + 2O$, with M^2 being the number of grid points inside the equator. The grid spacing Δ depends on M according to

$$\Delta = \frac{2}{M}. \tag{4.6}$$

The square grid determined by (4.5) ranges over

$$(\eta_i, \rho_j) \in (-1 - O\Delta, 1 + O\Delta) \tag{4.7}$$

in each patch.

In the original square patch method [30], the evolution algorithm is applied to the entire set of points in the square (η, ρ) grid, with the field values at the resulting ghost points supplied by interpolation from the other patch. In the circular patch method [28], the evolution algorithm is only applied to points inside a circle $r = \sqrt{\eta^2 + \rho^2}$, where $r > 1$ so that the boundary lies a small distance past the equator. In convergence tests, the number of overlap points determined by O is adjusted so that r is at a fixed position for all grids, i.e. O scales as $1/\Delta$. The grid points outside this circle are either ghost points or inactive. The circular patch is clearly more economical than using a square patch and avoids the error introduced by the large stereographic grid stretching near the corners of the square.

When the finite-difference stencil is used near the boundary of the active grid points, field values required at the ghost points outside a circular patch are interpolated from values at interior points of the opposite patch. The algorithm for determining the value of a scalar function F_N at a ghost point in the North patch starts with the determination of the ghost point's coordinates in the overlapping South patch, followed by the interpolation of the value of the function F_S at the ghost point, i.e. the F_N ghost point values are obtained by interpolation via the F_S active grid values.

Let R_E be the width of the finite-difference stencil divided by 2Δ. In the circular patch method, we define the *active* finite difference grid, i.e. the grid points to which the evolution algorithm is applied, by

$$\sqrt{\eta_i^2 + \rho_j^2} \le 1 + (O - R_E)\Delta, \tag{4.8}$$

where $O > R_E$. Stability of the composite mesh method requires that the interpolation stencil for the ghost points for one patch lies below the equator in the other patch. Those requirements give a minimum value of O but a larger value may be necessary to establish an effective buffer zone for the dissipation to attenuate the interpolation error before it enters the opposite patch. The optimum value of O in order to avoid instability or inaccuracy, needs to be established by experiment. (Too large a value would lead to inaccuracy due to the stretching of the stereographic grid.)

B. The cubed sphere

In the cubed-sphere approach, developed for meteorological studies in [29] and later for numerical relativity in [31], 6 coordinate patches on the sphere are obtained by projecting the 6 faces of a circumscribed cube. The method has recently been applied to characteristic evolution in [32] and independently in [33]. Here we follow the notation of [32], except we denote the angular coordinates by (ϕ_1, ϕ_2) (rather than by (ρ, σ)). In addition, in order to ensure that the coordinates and dyads on each patch are consistently right-handed, with the vector cross-product vector pointing out of the sphere, we introduce some sign changes in the conventions used in [32] for the coordinate transformations between the patches and in the definition of the dyad q^A.

These conventions simplify the interpatch transformation of spin-weighted quantities.

Given Cartesian coordinates (x, y, z), we define angular coordinates $x^A = (\phi_1, \phi_2)$ on the 2-sphere $x^2 + y^2 + z^2 = 1$ by means of the six patches $(x_\pm, y_\pm, z_\pm)$, where

$$\begin{aligned} x_\pm&: \ \phi_1 = \arctan\left(\pm\frac{y}{x}\right), \qquad \phi_2 = \arctan\left(\frac{z}{x}\right) \\ y_\pm&: \ \phi_1 = \arctan\left(\pm\frac{z}{y}\right), \qquad \phi_2 = \arctan\left(\frac{x}{y}\right) \\ z_\pm&: \ \phi_1 = \arctan\left(\pm\frac{x}{z}\right), \qquad \phi_2 = \arctan\left(\frac{y}{z}\right). \end{aligned} \tag{4.9}$$

In each patch, the range of the coordinates is $-\pi/4 \le \phi_1, \phi_2 \le \pi/4$ and the metric is

$$ds^2 = (1 - \sin^2\phi_1 \sin^2\phi_2)^{-2}\left(\cos^2\phi_2 d\phi_1^2 + \cos^2\phi_1 d\phi_2^2 - \frac{1}{2}\sin(2\phi_1)\sin(2\phi_2) d\phi_1 d\phi_2\right). \tag{4.10}$$

As a simple dyad representing (4.10), we choose

$$\begin{aligned} q_A &= \left(\frac{(\theta_c - i\theta_s)\cos\phi_2}{4\theta_c^2\theta_s^2}, \frac{(\theta_c + i\theta_s)\cos\phi_1}{4\theta_c^2\theta_s^2}\right), \\ q^A &= \left(2\theta_c\theta_s\frac{\theta_s - i\theta_c}{\cos\phi_2}, 2\theta_c\theta_s\frac{\theta_s + i\theta_c}{\cos\phi_1}\right), \end{aligned} \tag{4.11}$$

where

$$\theta_c = \sqrt{\frac{1 - \sin\phi_1\sin\phi_2}{2}}, \qquad \theta_s = \sqrt{\frac{1 + \sin\phi_1\sin\phi_2}{2}}. \tag{4.12}$$

The operator ð acting on a field S with spin-weight s is $ðS = q^A\partial_A S + s\Gamma S$ where, with the present conventions,

$$\begin{aligned} \Gamma = &\frac{\cos^2\phi_1\cos^2\phi_2(\sin\phi_1 + \sin\phi_2) + (\cos^2\phi_1 - \cos^2\phi_2)(\sin\phi_2 - \sin\phi_1)}{4\theta_c\cos\phi_2\cos\phi_1} \\ &- i\frac{\cos^2\phi_1\cos^2\phi_2(\sin\phi_1 - \sin\phi_2) + (\cos^2\phi_2 - \cos^2\phi_1)(\sin\phi_1 + \sin\phi_2)}{4\theta_s\cos\phi_2\cos\phi_1}. \end{aligned} \tag{4.13}$$

We introduce ghost zones in the usual manner along the boundaries of each patch, and couple the patches together by interpolating the field variables from neighboring patches to each ghost point. With the definition (4.9), the angular coordinate ϕ_1 or ϕ_2 perpendicular to an interpatch boundary is always common to both adjacent patches. This greatly simplifies interpatch interpolation, since it only needs to be done in 1 dimension, parallel to the boundary.

V. COMPARISON BETWEEN STEREOGRAPHIC AND CUBED-SPHERE METHODS

We carry out a test of wave propagation on the sphere to compare the accuracy of using circular stereographic patches with the cubed-sphere methods, with emphasis on the accuracy of the angular derivatives required in waveform extraction by the news and Ψ_4 approaches. The test allows direct comparison between the stereographic and cubed-sphere treatments without introducing the complications of characteristic evolution and the explicit calculations of the news or Ψ.

The test is based upon solutions to the 2D wave equation

$$-\partial_t^2\Phi + ð\bar{ð}\Phi = 0, \tag{5.1}$$

where $\Phi = \cos(\omega t)Y_{\ell m}$, $\omega = \sqrt{\ell(\ell+1)}$ and $Y_{\ell m}$ are spherical harmonics.

For the case $\ell = m = 2$, we compare test results for the stereographic grid with circular patches and the cubed-sphere grid. For the stereographic grid, the simulations are run with M^2 grid points in each patch, for $M = 100$ and $M = 120$. The corresponding cubed sphere runs keep the number of grid-cells covering the sphere the same as for the stereographic case, not counting those cells that overlap with another patch. For M^2 stereographic grid points there are $\approx \pi M^2/4$ grid-cells inside the equator on each hemisphere. In the cubed sphere grid, with N^2 points per patch, the entire sphere is covered by $6 \times N^2$ points. Equating the number of cells for the entire sphere gives $N^2 \approx (\pi/12)M^2$. The above values of M then correspond to $N = 51, 61$. The tests are run until $t = 120$.

Angular dissipation is necessary for the stability of the stereographic runs. For grid size Δ, it was added in the finite-difference form

$$\partial_t^2\Phi \rightarrow \partial_t^2\Phi + \epsilon\Delta^3\mathcal{D}^4\partial_t\Phi, \tag{5.2}$$

where $\mathcal{D}^4\Phi = (\frac{p^2}{4}(\mathcal{D}_{+\eta}\mathcal{D}_{-\eta} + \mathcal{D}_{+\rho}\mathcal{D}_{-\rho}))^2\Phi$, where $\mathcal{D}_+$ (or $\mathcal{D}_-$) indicates the forward (or backward) difference operator in the indicated direction. Experimentation with tuning the dissipation revealed that a small value $\epsilon = 0.01$ is sufficient to suppress high frequency error. The finite-difference stencil (taking dissipation into account) has width $R_E = 2$. Using a 4th order Lagrange interpolator and by tuning the number O of overlapping points, we obtained good results with $O = 5$. Angular dissipation was not used in the cubed sphere runs.

TABLE I. Convergence rates for $\mathcal{E}(\Phi)$, obtained with the L_∞ norm using the $M = 100$ and $M = 120$ grids.

ALGORITHM	$t = 1.2$	$t = 12$	$t = 102$	$t = 120$
circular patch	2.002	1.988	1.994	1.999
cubed-sphere	1.994	1.970	1.982	1.985

We use the L_∞ norm to measure the error

$$\mathcal{E}(\Phi) = \|\Phi_{\text{numeric}} - \Phi_{\text{analytic}}\|_\infty. \tag{5.3}$$

We measure the convergence rate for $\mathcal{E}(\Phi)$ at a given time t, for two grid sizes Δ_1 and Δ_2, by

$$\mathcal{R} = \frac{\log_2(\mathcal{E}(\Phi)_{\Delta_1}/\mathcal{E}(\Phi)_{\Delta_2})}{\log_2(\Delta_2/\Delta_1)}. \tag{5.4}$$

Convergence rates for other quantities are measured analogously. For a given grid, we measure the error for the circular patches in the North hemisphere; while for the cubed-sphere method we measure the error on the $(+x, +y, +z)$ patch, excluding ghost points at the edges of the patch. The finite difference approximations for the codes are designed to be second order accurate.

Excellent second-order convergence of $\mathcal{E}(\Phi)$, based upon the $M = 100$ and $M = 120$ grids, is evident for both methods from the results listed in Table I. The time dependence of the error plots in Fig. 1, shows that the cubed-sphere error is $\approx \frac{1}{3}$ the stereographic error.

A more important test to assess the error relevant to gravitational wave extraction is to measure the error in $\eth^2\Phi$, since second angular derivatives enter in the computation of the Bondi news. The convergence rates, measured with the L_∞ norm, are shown in Table II. The circular patch and cubed-sphere results indicate clean second order convergence up to the final run time at $t = 120$. The plots of the error versus time in Fig. 2 show that the error for the cubed-sphere is about $\frac{2}{3}$ the stereographic error.

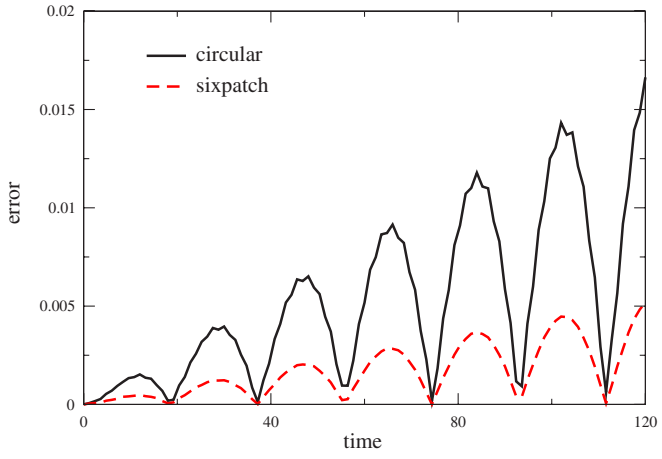

FIG. 1 (color online). Comparison of the L_∞ error $\mathcal{E}(\Phi)$ vs t, for the highest resolution runs using the circular patch method and the cubed-sphere method.

TABLE II. Convergence rates for the L_∞ error $\mathcal{E}(\eth^2\Phi)$ for various times t, obtained using the two highest resolution runs.

ALGORITHM	$t = 1.2$	$t = 12$	$t = 102$	$t = 120$
circular patch	2.022	1.945	1.992	2.006
cubed-sphere	1.954	2.019	1.997	1.971

Similarly, it is important for the purpose of gravitational wave extraction using the Weyl tensor to measure the error in $\bar{\eth}\eth^2\Phi$, since third angular derivatives enter into the computation of Ψ. The corresponding convergence rates are shown in Table III. Now the cubed-sphere method shows poor convergence of the L_∞ error at early times. The underlying error is generated at the corners where three patches meet, as indicated by the improved conver-

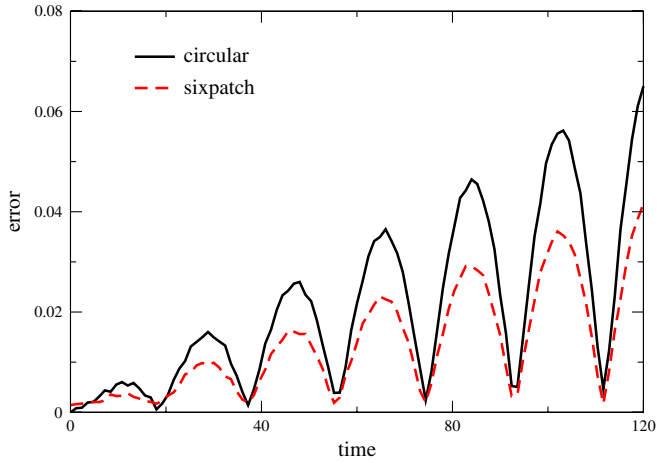

FIG. 2 (color online). The L_∞ error $\mathcal{E}(\eth^2\Phi)$ vs t for the highest resolution runs is compared using the circular patch method and the cubed-sphere method.

TABLE III. Convergence rates for the error $\mathcal{E}(\bar{\eth}\eth^2\Phi)$. For the cubed-sphere method the dominant error arises at the patch corners, which is revealed by the comparison of the L_∞ and L_2 errors. This can be understood in terms of the interpatch interpolation stencil which is partially off-centered near the corners, where the error is greatest. The inherent numerical dissipation of the evolution algorithm keeps this localized, nonsmooth noise from growing, while smoother error from other regions grows linearly in time (see Fig. 3). The net effect is that at late times both the L_∞ and the L_2 norms of the error in the third derivative show second order convergence, while early in the evolution the L_∞ shows only first order convergence.

ALGORITHM	$t = 1.2$	$t = 12$	$t = 102$	$t = 120$
circular patch, L_∞ norm	2.278	2.032	1.988	2.009
cubed-sphere, L_∞ norm	1.108	0.882	2.009	1.959
cubed-sphere, L_2 norm	1.883	1.983	1.981	1.959

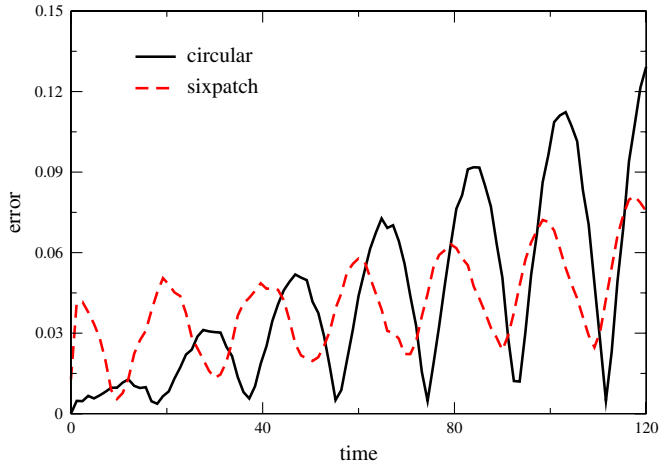

FIG. 3 (color online). The error $\mathcal{E}(\bar{\eth}\bar{\eth}^2\Phi)$ vs t is compared for the highest resolution runs using the circular patch method and the cubed-sphere method.

gence rate measured using the L_2 norm. Apparently some built-in dissipation of the evolution algorithm smooths this patch-boundary error and second order convergence is evident by $t = 102$. To a much smaller extent, the L_∞ error for the circular patch method also shows some deviation from second order convergence at early times, but clean second order convergence is evident by $t = 12$.

The magnitude of the L_∞ error in $\bar{\eth}\bar{\eth}^2\Phi$ is plotted vs time in Fig. 3. Until about $t = 60$, the cubed-sphere method has the largest error. But at the end of the run at $t = 120$ the cubed-sphere error is about $\frac{4}{5}$ the stereographic error.

Surface plots of the error at the final run time are shown in Fig. 4. The circular patch and cubed-sphere errors are both smooth, as would be expected of the second order truncation error arising from the finite differencing. For the circular patch, this shows that dissipation in the buffer zone surrounding the equator effectively guards against the high frequency error introduced at the patch boundary. Our results for the stereographic method justify its use in the comparison of the news and Weyl tensor extraction strategies in Sec. VI.

VI. COMPARISON OF NEWS AND WEYL TENSOR EXTRACTION

Here we compare the accuracy of waveform extraction by computing the news function N or the Weyl tensor component Ψ in a linearized gravitational wave test problem. The computations are carried out by the procedure described in Sec. III D. In accord with (3.49), the Ψ computation yields an alternative numerical value for the news

$$N_\Psi = N|_{u=0} + \int_0^u \Psi du, \tag{6.1}$$

where $N = N_\Psi$ in the analytic problem. We compare the two extraction methods in terms of the errors in N and N_Ψ obtained using the stereographic method.

We base the test on a class of solutions in Bondi-Sachs form to the linearized vacuum Einstein equation on a Minkowski background given in Sec. 4.3 of [42]. The solution allows us to make convergence checks of the Bondi-Sachs metric quantities as well as the news function. The solutions are expressed in terms of spin-weighted spherical harmonics ${}_sY_{\ell m}$ [36,43], modified to avoid mixing of the m and $-m$ components when extracting the real part according to [44]

$$\begin{aligned} {}_sR_{\ell m} &= \frac{1}{\sqrt{2}}[{}_sY_{\ell m} + (-1)^m {}_sY_{\ell -m}] \quad \text{for } m > 0, \\ {}_sR_{\ell m} &= \frac{i}{\sqrt{2}}[(-1)^m {}_sY_{\ell m} - {}_sY_{\ell -m}] \quad \text{for } m < 0, \\ {}_sR_{\ell 0} &= {}_sY_{\ell 0}. \end{aligned} \tag{6.2}$$

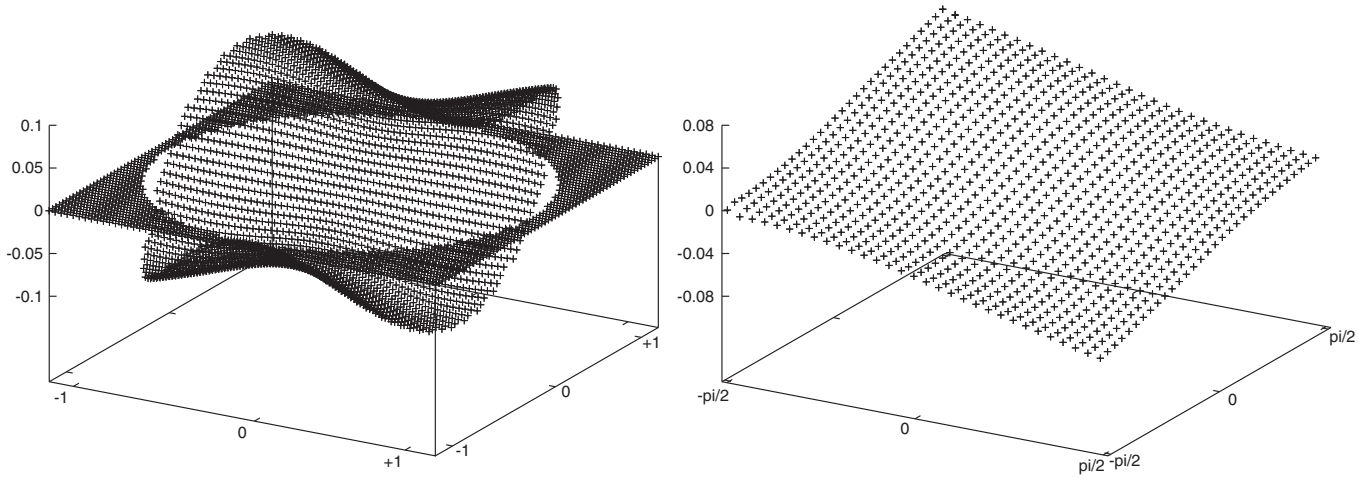

FIG. 4. 2D snapshots of the error in $\bar{\eth}\bar{\eth}^2\Phi$ at $t = 120$ for the on the North hemisphere for the circular patch method (left plot), and for a cubed-sphere patch (right plot). For the sake of plot clarity these 2D snapshots use only every third data-point along each axis. The third angular derivatives are smooth for both methods.

Ref. [44] gives explicit expressions for the ${}_sR_{\ell m}$ in stereographic coordinates.

Following [32], these linearized solutions have Bondi-Sachs variables

$$\begin{aligned} J &= \sqrt{(\ell-1)\ell(\ell+1)(\ell+2)}\,{}_2R_{\ell m}\Re(J_\ell(r)e^{i\nu u}),\\ U &= \sqrt{\ell(\ell+1)}\,{}_1R_{\ell m}\Re(U_\ell(r)e^{i\nu u}),\\ \beta &= R_{\ell m}\Re(\beta_\ell e^{i\nu u}),\\ W_c &= R_{\ell m}\Re(W_{c\ell}(r)e^{i\nu u}), \end{aligned} \tag{6.3}$$

where W_c determines the perturbation in V. Here $J_\ell(r)$, $U_\ell(r)$, β_ℓ, $W_{c\ell}(r)$ are in general complex, and taking the real part leads to $\cos(\nu u)$ and $\sin(\nu u)$ terms. The quantities β and W_c are real, while J and U are complex. We require a solution that is well-behaved at future null infinity, and is well-defined for $r \geq r_0 > 0$, where r_0 is the inner boundary. We find in the case $\ell = 2$

$$\begin{aligned} \beta_2 &= \beta_0\\ J_2(r) &= \frac{24\beta_0 + 3i\nu C_1 - i\nu^3 C_2}{36} + \frac{C_1}{4r} - \frac{C_2}{12r^3}\\ U_2(r) &= \frac{-24i\nu\beta_0 + 3\nu^2 C_1 - \nu^4 C_2}{36} + \frac{2\beta_0}{r} + \frac{C_1}{2r^2}\\ &\quad + \frac{i\nu C_2}{3r^3} + \frac{C_2}{4r^4}\\ W_{c2}(r) &= \frac{24i\nu\beta_0 - 3\nu^2 C_1 + \nu^4 C_2}{6}\\ &\quad + \frac{3i\nu C_1 - 6\beta_0 - i\nu^3 C_2}{3r} - \frac{\nu^2 C_2}{r^2} + \frac{i\nu C_2}{r^3} + \frac{C_2}{2r^4}, \end{aligned} \tag{6.4}$$

with the (complex) constants β_0, C_1 and C_2 freely specifiable. In the case $\ell = 3$

$$\begin{aligned} \beta_2 &= \beta_0\\ J_3(r) &= \frac{60\beta_0 + 3i\nu C_1 + \nu^4 C_2}{180} + \frac{C_1}{10r} - \frac{i\nu C_2}{6r^3} - \frac{C_2}{4r^4}\\ U_3(r) &= \frac{-60i\nu\beta_0 + 3\nu^2 C_1 - i\nu^5 C_2}{180} + \frac{2\beta_0}{r} + \frac{C_1}{2r^2}\\ &\quad - \frac{2\nu^2 C_2}{3r^3} + \frac{5i\nu C_2}{4r^4} + \frac{C_2}{r^5}\\ W_{c3}(r) &= \frac{60i\nu\beta_0 - 3\nu^2 C_1 + i\nu^5 C_2}{15} + \frac{i\nu C_1 - 2\beta_0 + \nu^4 C_2}{3r}\\ &\quad - \frac{i2\nu^3 C_2}{r^2} - \frac{4i\nu^2 C_2}{r^3} + \frac{5\nu C_2}{r^4} + \frac{3C_2}{r^5}. \end{aligned} \tag{6.5}$$

The news N for the linearized wave is given by

$$\begin{aligned} N = \Re\Big(e^{i\nu u}\lim_{r\to\infty}\Big(-\frac{\ell(\ell+1)}{4}J_\ell - \frac{i\nu}{2}r^2 J_{\ell,r}\Big) + e^{i\nu u}\beta_\ell\Big)\\ \times\sqrt{(\ell-1)\ell(\ell+1)(\ell+2)}\,{}_2R_{\ell m}, \end{aligned} \tag{6.6}$$

corresponding For the cases $\ell = 2$ and 3, this gives

$$\begin{aligned} \ell = 2\text{: } N &= \Re\Big(\frac{i\nu^3 C_2}{\sqrt{24}}e^{i\nu u}\Big){}_2R_{2m};\\ \ell = 3\text{: } N &= \Re\Big(\frac{-\nu^4 C_2}{\sqrt{30}}e^{i\nu u}\Big){}_2R_{3m}. \end{aligned} \tag{6.7}$$

For the linearized case $\Psi = N_{,u}$, which gives

$$\begin{aligned} \ell = 2\text{: } \Psi &= \Re\Big(\frac{-\nu^4 C_2}{\sqrt{24}}e^{i\nu u}\Big){}_2R_{2m};\\ \ell = 3\text{: } \Psi &= \Re\Big(\frac{-i\nu^5 C_2}{\sqrt{30}}e^{i\nu u}\Big){}_2R_{3m}. \end{aligned} \tag{6.8}$$

A. Test specifications

Tests were run with the solution parameters $\nu = 1$ and $m = 0$ for the cases $\ell = 2$ and $\ell = 3$, with

$$\begin{aligned} C_1 &= 3\cdot 10^{-6}, \qquad C_2 = 10^{-6},\\ \beta_0 &= i\cdot 10^{-6} \qquad (\ell = 2) \end{aligned} \tag{6.9}$$

$$\begin{aligned} C_1 &= 3\cdot 10^{-6}, \qquad C_2 = i\cdot 10^{-6},\\ \beta_0 &= i\cdot 10^{-6} \qquad (\ell = 3). \end{aligned} \tag{6.10}$$

The inner worldtube boundary was placed at $r_0 = 2$ corresponding to a compactified radial coordinate $x_0 = r_0/(R + r_0) \approx .1888$, where we have set the scale parameter $R = 9$.

For the convergence measurements, the (η, ρ, x) grid consisted of M^3 points, with $M = 100$ and $M = 120$. The boundary of the circular patches were fixed at $\sqrt{\eta^2 + \rho^2} = 1.4$. The runs were stopped at $t = 100$. The L_∞ and L_2 error norms were computed on the North hemisphere, using the values from the North patch.

Angular dissipation was applied only to the circular patch runs, with the dissipation coefficients $\epsilon_x = 0.009$, $\epsilon_u = 0.0009$, and $\epsilon_Q = \epsilon_W = 0.00001$. The weighting function $\mathcal{W}$ for application of the dissipation was taken to be a unit step function which vanishes for $\sqrt{\eta^2 + \rho^2} \geq 1.3$.

We present output data for the real parts of J, N, and N_Ψ. For the $m = 0$ case, these quantities correspond to a pure $\oplus$ polarization mode. For comparison purposes, we include results for the circular patch without dissipation and the original square patch treatment.

B. Test results for J

We first present test results for J, which is a typical metric quantity entering into the waveform calculation. Figure 5 show the L_∞ norm over the North hemisphere of the error $\mathcal{E}(J)$ vs the compactified radial coordinate x at the end of the run at $t = 100$ for the $\ell = 2$ wave. The figure compares runs made with the circular patch method (dis-

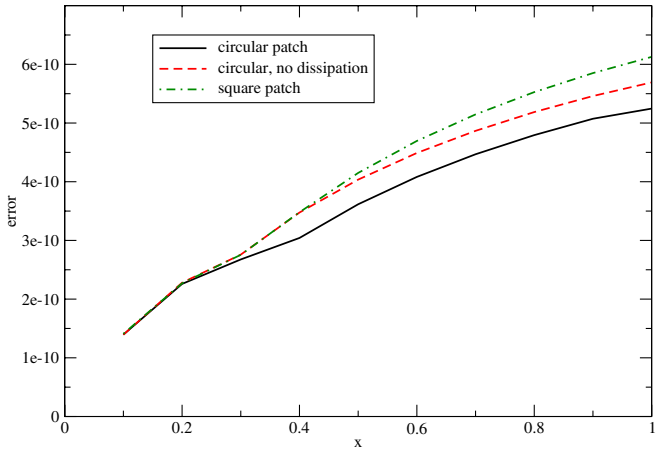

FIG. 5 (color online). The L_∞ error $\mathcal{E}(J)$ plotted vs x at $t = 100$ for runs with the circular patch method (with and without dissipation) and with the square patch method.

sipation applied) with runs without dissipation and runs with the original square patch method. The plots show that angular dissipation reduces the error. This will become more evident in the later test results for the news in which higher angular derivatives are involved. An important feature of the plots is that in all cases the error increases monotonically and takes it maximum value at $\mathcal{I}^+$ ($x = 1$), as would be expected of the radial marching algorithm. This allows us to focus our error analysis on output at $\mathcal{I}^+$.

Table IV gives the convergence rate of the error in J measured at $\mathcal{I}^+$ at various times during the $\ell = 2$ run for the three methods shown in Fig. 5. Clean second order convergence, measured either with an L_2 or L_∞ norm, is indicated in all cases. The corresponding convergence rates for the $\ell = 3$ runs are given in Table V. The $\ell = 2$ runs are more discriminating because $|J|$ has a $\sin^2\theta$ dependence which peaks at the equator close to the interpatch interpolation, as opposed to the $\sin^2\theta\cos\theta$ dependence of the $\ell = 3$ case which vanishes at the equator. In the following we restrict our discussion to the $\ell = 2$ case.

The time dependence of the L_2 and L_∞ errors in J at $\mathcal{I}^+$ for the circular patch run (with dissipation) is plotted in

TABLE IV. Convergence rates of the error $\mathcal{E}(J)$ at $\mathcal{I}^+$ for the $\ell = 2$ run, measured at times $t = 1$, $t = 10$, $t = 90$, and $t = 100$.

Variable	circular patch	circular, no dissipation	square patch
$\mathcal{E}_{L_2}(J)_{t=1}$	2.01	2.00	2.01
$\mathcal{E}_{L_2}(J)_{t=10}$	2.01	1.98	2.00
$\mathcal{E}_{L_2}(J)_{t=90}$	2.00	2.02	2.02
$\mathcal{E}_{L_2}(J)_{t=100}$	1.92	2.03	2.00
$\mathcal{E}_{L_\infty}(J)_{t=1}$	2.01	2.01	2.01
$\mathcal{E}_{L_\infty}(J)_{t=10}$	1.95	2.00	1.99
$\mathcal{E}_{L_\infty}(J)_{t=90}$	2.07	1.96	2.00
$\mathcal{E}_{L_\infty}(J)_{t=100}$	1.92	2.01	1.99

TABLE V. Convergence rates of the error $\mathcal{E}(J)$ at $\mathcal{I}^+$ for the $\ell = 3$ run, measured at times $t = 1$, $t = 10$, $t = 90$, and $t = 100$.

Variable	circular patch	circular, no dissipation	square patch
$\mathcal{E}_{L_2}(J)_{t=1}$	2.02	2.01	2.01
$\mathcal{E}_{L_2}(J)_{t=10}$	2.00	2.00	2.00
$\mathcal{E}_{L_2}(J)_{t=90}$	2.03	2.02	2.02
$\mathcal{E}_{L_2}(J)_{t=100}$	2.05	2.00	2.01
$\mathcal{E}_{L_\infty}(J)_{t=1}$	2.02	2.02	2.02
$\mathcal{E}_{L_\infty}(J)_{t=10}$	1.99	1.99	2.00
$\mathcal{E}_{L_\infty}(J)_{t=90}$	2.02	2.02	2.04
$\mathcal{E}_{L_\infty}(J)_{t=100}$	2.00	2.00	1.99

Fig. 6. The plots are based upon output at integer values of t, which samples the error at various phases during the underlying period $T = 2\pi$. The errors for the two grids used in the convergence measurements are rescaled to the values for the finest $M = 120$ grid, with the overlap again confirming clean convergence. The magnitude of the error is approximately 0.1% the value of J. The L_2 error is smaller than the L_∞ because the error is sharply peaked near the equator. This error pattern in the North hemisphere is exhibited in the snapshot of Fig. 7 at $t = 100$. The profile is quite smooth—some of the apparent jaggedness near the edge is an artificial effect of the irregular pattern of grid points at the edge of the equator. The sharp spikes in the corresponding error snapshot for the circular run without dissipation shown in Fig. 8 illustrate the essential role of angular dissipation in guarding the Northern hemisphere from the interpolation error at the circular patch boundary. Such spikes are not apparent in the corresponding error snapshot for the square patch shown in Fig. 9. The more regular square patch boundary does not require angular dissipation, although the resulting error is larger than for the circular patch with dissipation.

C. Test results for the news

We now compare test results for the news function in terms of a direct calculation of N via (3.21) and a calculation of N_Ψ via (6.1) using the Weyl component Ψ given in (3.41). We restrict the discussion to the $\ell = 2$ runs which are more challenging than $\ell = 3$ with respect to problems near the equator. Tables VI and VII give the convergence rates of the L_2 and L_∞ errors in N and N_Ψ measured at various times for runs with the circular patch (with dissipation), the circular patch without dissipation and the original square patch methods. At the final run time $t = 100$, measurements for all cases show clean second order convergence, although there is a small departure in the N_Ψ rates at early times.

The plots of the L_2 error vs time for the circular patch runs in Fig. 10 show little difference in the time behavior between N and N_Ψ, although the error in N_Ψ is slightly smaller. The L_∞ errors measured at the end of the runs on

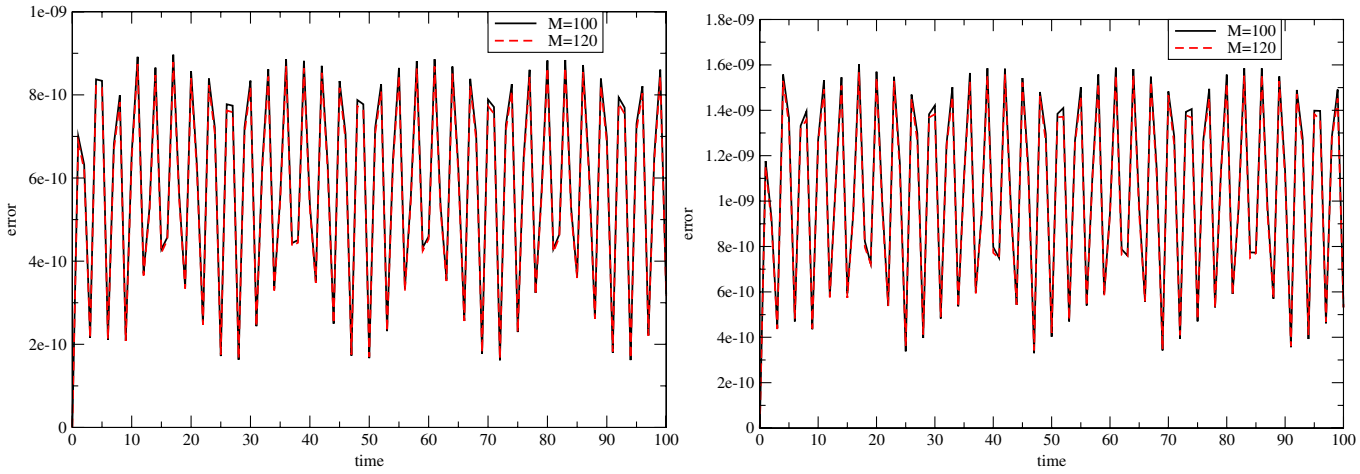

FIG. 6 (color online). Plots of the error $\mathcal{E}(J)$ at $\mathcal{I}^+$ vs t, for the circular patch with dissipation measured with the L_2 norm (left plot) and the L_∞ norm (right plot). The error for the $M = 100$ grid is rescaled and overlaid on the error for the $M = 120$ grid to exhibit the second order convergence. The smaller L_2 error indicates that the maximum error arises near the equator.

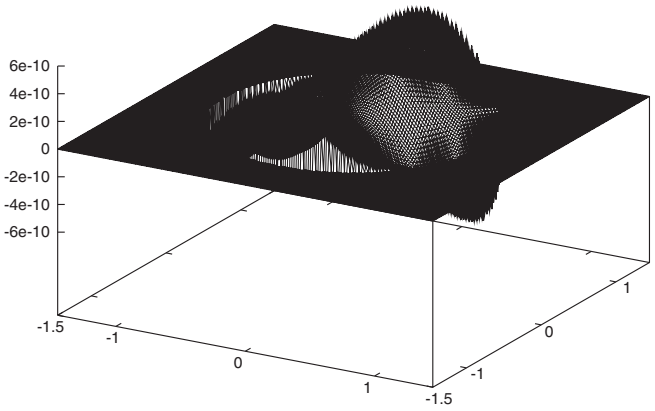

FIG. 7. Surface plot of the error in J at $t = 100$ for the circular patch run (with dissipation).

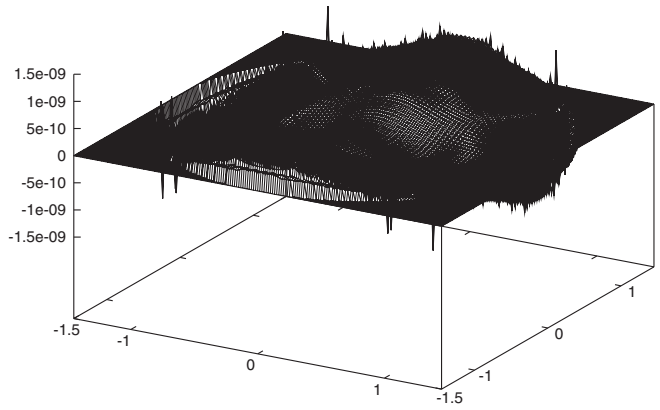

FIG. 8. Surface plot of the error in J at $t = 100$ for the circular patch run without dissipation.

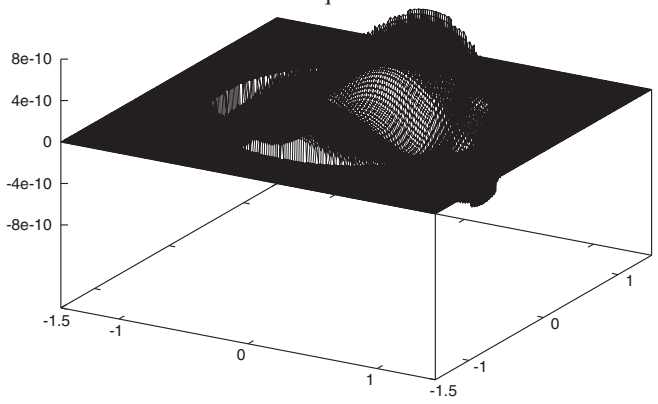

FIG. 9. Surface plot of the error in J at $t = 100$ for the square patch run.

TABLE VI. Convergence rates of the error $\mathcal{E}(N)$, measured at $t = 1$, $t = 10$, $t = 90$, and $t = 100$.

Variable	circular patch	circular, no dissipation	square patch
$\mathcal{E}_{L_2}(N)_{t=1}$	2.05	2.05	2.05
$\mathcal{E}_{L_2}(N)_{t=10}$	2.05	2.05	2.04
$\mathcal{E}_{L_2}(N)_{t=90}$	2.04	2.04	2.01
$\mathcal{E}_{L_2}(N)_{t=100}$	2.01	2.07	2.05
$\mathcal{E}_{L_\infty}(N)_{t=1}$	2.04	2.04	2.04
$\mathcal{E}_{L_\infty}(N)_{t=10}$	2.04	1.99	2.04
$\mathcal{E}_{L_\infty}(N)_{t=90}$	2.01	2.01	2.06
$\mathcal{E}_{L_\infty}(N)_{t=100}$	1.98	2.00	1.93

TABLE VII. Convergence rates of the error $\mathcal{E}(N_\Psi)$, measured at $t = 1$, $t = 10$, $t = 90$, and $t = 100$.

Variable	circular patch	circular, no dissipation	square patch
$\mathcal{E}_{L_2}(N_\Psi)_{t=1}$	2.11	2.10	2.11
$\mathcal{E}_{L_2}(N_\Psi)_{t=10}$	2.13	2.13	2.11
$\mathcal{E}_{L_2}(N_\Psi)_{t=90}$	2.09	2.09	2.08
$\mathcal{E}_{L_2}(N_\Psi)_{t=100}$	2.02	1.98	2.00
$\mathcal{E}_{L_\infty}(N_\Psi)_{t=1}$	2.08	2.08	2.08
$\mathcal{E}_{L_\infty}(N_\Psi)_{t=10}$	2.09	2.05	2.10
$\mathcal{E}_{L_\infty}(N_\Psi)_{t=90}$	2.05	2.00	2.06
$\mathcal{E}_{L_\infty}(N_\Psi)_{t=100}$	1.98	2.01	1.93

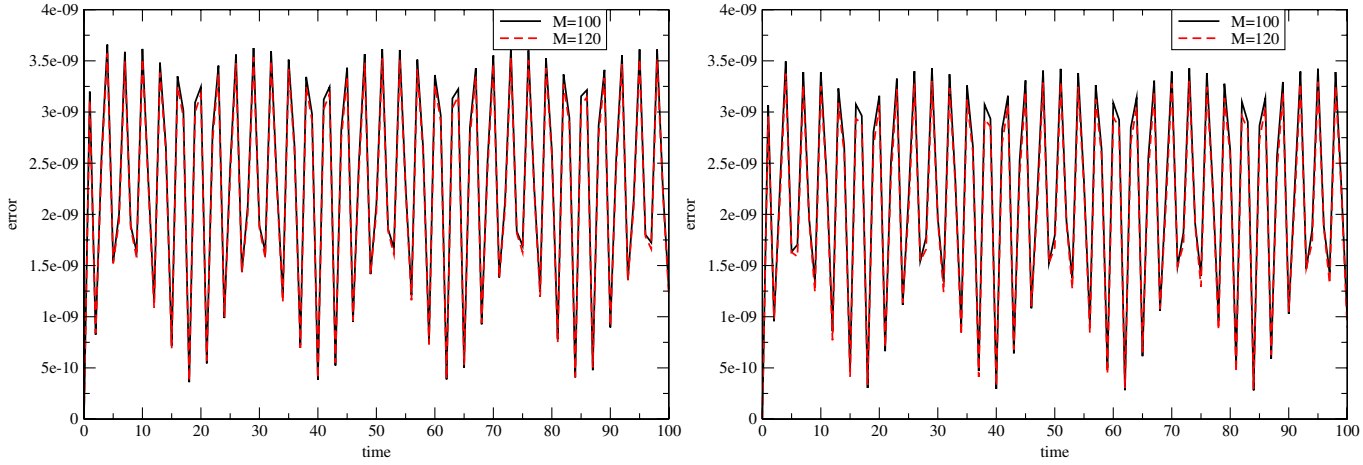

FIG. 10 (color online). Plots of the L_2 errors vs t for N (left plot) and N_Ψ (right plot) for the circular patch runs. The plots for the $M = 100$ grid are rescaled to the $M = 120$ grid. The plots are based upon output at integer values of t.

TABLE VIII. The values of the L_∞ errors in N and N_Ψ measured at $t = 100$.

Variable	circular patch	circular, no dissipation	square patch
$\mathcal{E}_{L_\infty}(N)$	2.247×10^{-9}	3.325×10^{-9}	2.897×10^{-9}
$\mathcal{E}_{L_\infty}(N_\Psi)$	1.706×10^{-9}	2.747×10^{-9}	2.315×10^{-9}

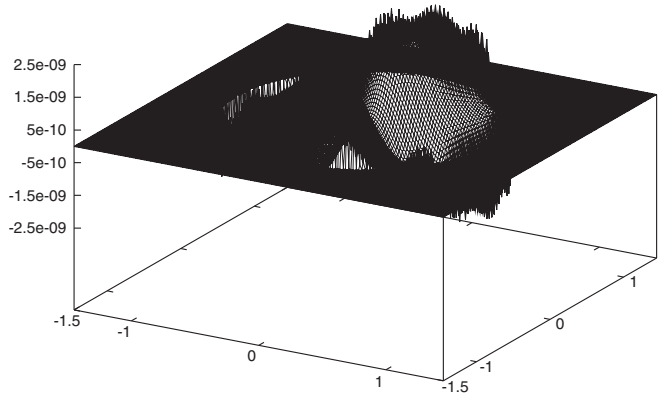

FIG. 11. Surface plot of the error in N at $t = 100$ for the circular patch.

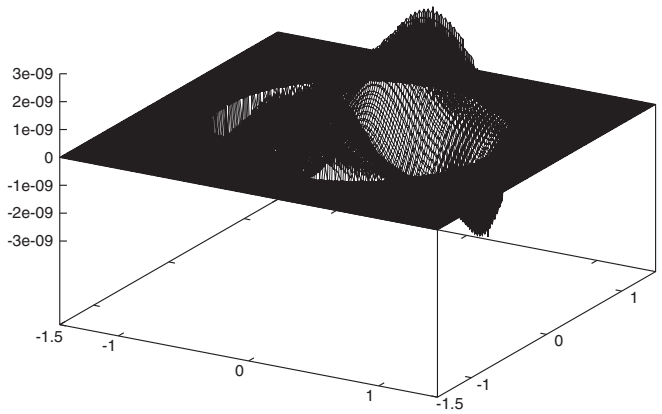

FIG. 12. Surface plot of the error in N at $t = 100$ for the square patch.

the $M = 120$ grid are given in Table VIII for the circular patch, the circular patch without dissipation and the square patch. The best results are obtained for the circular patch, which shows an $\approx 30\%$ improvement over the original square patch treatment. The results also show the essential improvement due to the use of angular dissipation. For the circular patch, the error in N_Ψ was $\approx 24\%$ smaller than the error in N at the end of the run. But it is also clear from the plots of the L_2 error in Fig. 10 that this ratio depends when and where this ratio is taken. At the equator where the news takes its maximum value, its modulus for this test is $|N_{\text{analytic}}| \approx 8 \times 10^{-8}$. At the end of run, the corresponding fractional errors in N_Ψ and N are $\approx 4\%$ for averaged values and $\approx 9\%$ for the maximum errors at the equator.

Surface plots of the error in N and N_Ψ at the end of the run are given in Figs. 11–14 for the circular and square patches. The lack of sharp spikes in the errors for the circular patches shows the effectiveness of applying angular dissipation. There is slightly more jaggedness near the equator for the circular vs square patch errors, but this is overbalanced by the relative smallness of the circular patch error.

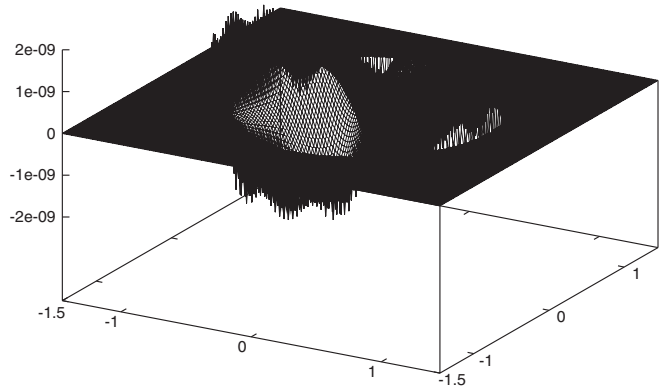

FIG. 13. Surface plot of the error in N_Ψ at $t = 100$ for the circular patch.

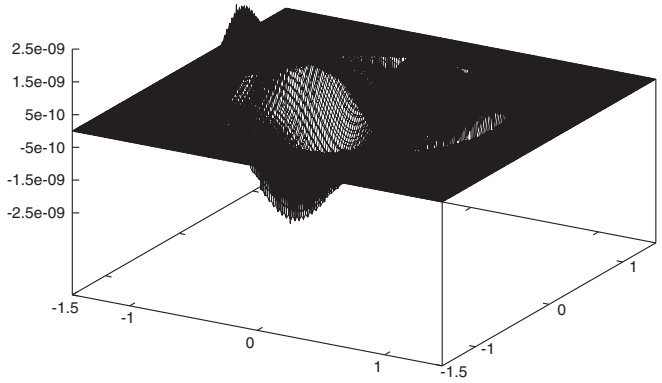

FIG. 14. Surface plot of the error in N_Ψ at $t = 100$ for the square patch.

VII. CONCLUSION

We have proposed two new methods for enhancing the accuracy of CCE, One is a numerical method modifying the stereographic patches used in the characteristic evolution code to conform to the circular patch boundaries as used in meteorology [28]. The other is a geometrical method that bases the waveform on the limiting behavior at $\mathcal{I}^+$ of the Weyl tensor component Ψ_4 rather than the news function.

We have used a scalar wave test bed to compare the circular patch method against the cubed-sphere method, which is also extensively used in meteorology [29]. We found, for equivalent computational expense, that the cubed-sphere method has an edge in accuracy over the stereographic method. The cubed-sphere error in the scalar field $\mathcal{E}(\Phi)$ is $\approx \frac{1}{3}$ the stereographic error but that the advantage is smaller for the higher derivatives required in gravitational waveform extraction. The cubed-sphere error $\mathcal{E}(\tilde{\eth}\eth^2\Phi)$ is only $\approx \frac{4}{5}$ the stereographic error. An advantage of the stereographic approach is its relative programming simplicity. But as originally pointed out in [29], and demonstrated recently for the case of a characteristic evolution code [33], once all the necessary infrastructure for interpatch communication is in place, the shared boundaries of the cubed-sphere approach admit a highly scalable algorithm for parallel architectures.

We used the circular patch stereographic code to compare waveform extraction in a linearized wave test directly via the Bondi news function N and its counterpart N_Ψ constructed from the Weyl curvature. For this purpose, we were able to successfully implement a new form of angular dissipation in the characteristic evolution code, which otherwise would be prone to high frequency error introduced by the irregular way a circular boundary cuts through a square grid. Our test results show that this dissipation works: the resulting error in the waveforms and metric quantities is smooth. In addition, the extensive analytic and numerical manipulations carried out to compute the limiting behavior of the Weyl curvature was demonstrated to yield second order accurate results for N_Ψ.

In the linearized tests presented here, neither N nor N_Ψ was a clear winner. We already knew that the original news module based upon a square stereographic patch worked well in the linear regime. The news N calculated on a circular patch had lower error than that on a square patch but only by a $\approx 30\%$ factor. In turn, the news calculated via N_Ψ on the circular patch had a lower error than N on the circular patch by a $\approx 24\%$ factor. Weyl tensor extraction is slightly more accurate than news function extraction, even though there are many more terms involved.

All errors were second order convergent. However, while there was a small fractional error $\approx .1\%$ in metric quantities such as J, the corresponding averaged error in the N_Ψ and N was $\approx 4\%$ for the circular patch runs and the maximum error at the equator was $\approx 9\%$. These errors did not vary appreciably ($\approx 30\%$) with the choice of discretization method, i.e. circular patch or square patch. They reflect the intrinsic difficulty in extracting waveforms due to the delicate cancellation of leading order terms in the underlying metric and connection when computing $O(1/r)$ quantities such as Ψ_4. The excellent accuracy that we find for the metric suggests that perturbative waveform extraction must suffer the same difficulty. In that case it is just less obvious how to quantify the errors. The delicate issues involved at $\mathcal{I}^+$ have been shown to have counterparts in extraction on a finite worldtube [24].

Waveforms are not easy to extract accurately. However, the convergence of our error measurements is a positive sign that higher order finite difference approximations might supply the accuracy that is needed for realistic astrophysical applications. Whether the advantages the new methods proposed here prove to be significant will depend upon the results of future application in the nonlinear regime.

ACKNOWLEDGMENTS

We thank Thomas Maedler for checking the calculations in Sec. III B and G. L. Browning for correspondence concerning the application of stereographic patches in computational fluid dynamics. N. T. B. thanks Max-Planck-Institut für Gravitationsphysik, Albert-Einstein-Institut for hospitality; B. S. thanks University of South Africa for hospitality; and M. C. B. thanks University of Pittsburgh for hospitality. We have benefited from the use of the Cactus Computational Toolkit (http://www.cactuscode.org). Computer time was provided by the Pittsburgh Supercomputing Center through TeraGrid Wide Roaming Access Computational Resources , and we owe special thanks to R. Gómez for his assistance. This work was supported by the Sherman Fairchild Foundation and the National Science Foundation under grants PHY-061459 and PHY-0652995 to the California Institute of Technology; the National Science Foundation grant PH-0553597 to the University of Pittsburgh; and by the National Research Foundation, South Africa, under GUN 2075290.

[1] H. Bondi, M. J. G. van der Burg, and A. W. K. Metzner, Proc. R. Soc. A **269**, 21 (1962).
[2] R. K. Sachs, Proc. R. Soc. A **270**, 103 (1962).
[3] R. Penrose, Phys. Rev. Lett. **10**, 66 (1963).
[4] R. A. Isaacson, J. S. Welling, and J. Winicour, J. Math. Phys. (N.Y.) **24**, 1824 (1983).
[5] N. T. Bishop, R. Gómez, L. Lehner, M. Maharaj, and J. Winicour, Phys. Rev. D **56**, 6298 (1997).
[6] N. T. Bishop, R. Gómez, L. Lehner, and J. Winicour, Phys. Rev. D **54**, 6153 (1996).
[7] H. Friedrich, Lect. Notes Phys. **604**, 1 (2002).
[8] S. Husa, Lect. Notes Phys. **617**, 159 (2003).
[9] J. Frauendiener, Living Rev. Relativity **7**, 253 (2004).
[10] N. T. Bishop, R. Gómez, L. Lehner, B. Szilágyi, J. Winicour, and R. A. Isaacson, in *Black Holes, Gravitational Radiation and the Universe*, edited by B. Iyer and B. Bhawal (Kluwer Academic Publishers, Dordrecht, 1998).
[11] J. Winicour, Living Rev. Relativity **8**, 10 (2005).
[12] B. Szilágyi and J. Winicour, Phys. Rev. D **68**, 041501 (2003).
[13] B. Gustaffson and H.-O. Kreiss, J. Comput. Phys. **30**, 333 (1979).
[14] H. Friedrich and G. Nagy, Commun. Math. Phys. **201**, 619 (1999).
[15] E. T. Newman and R. Penrose, J. Math. Phys. (N.Y.) **3**, 566 (1962).
[16] O. Rinne, L. Lindblom, and M. A. Scheel, Classical Quantum Gravity **24**, 4053 (2007).
[17] T. Regge and J. A. Wheeler, Phys. Rev. **108**, 1063 (1957).
[18] F. Zerilli, Phys. Rev. Lett. **24**, 737 (1970).
[19] A. Nagar and L. Rezzolla, Classical Quantum Gravity **22**, R167 (2005).
[20] J. Baker, M. Campanelli, C. O. Lousto, and R. Takahashi, Phys. Rev. D **65**, 124012 (2002).
[21] F. Pretorius, Phys. Rev. Lett. **95**, 121101 (2005).
[22] M. Campanelli, C. O. Lousto, P. Marronetti, and Y. Zlochower, Phys. Rev. Lett. **96**, 111101 (2006)
[23] J. G. Baker, J. Centrella, D-I. Choi, M. Koppitz, and J. van Meter, Phys. Rev. D **73**, 104002 (2006).
[24] L. Lehner and O. M. Moreschi, Phys. Rev. D **76**, 124040 (2007).
[25] M. Babiuc, B. Szilágyi, I. Hawke, and Y. Zlochower, Classical Quantum Gravity **22**, 5089 (2005).
[26] N. T. Bishop, R. Gómez, S. Husa, L. Lehner, and J. Winicour, Phys. Rev. D **68**, 084015 (2003).
[27] F. Pretorius and L. Lehner, J. Comput. Phys. **198**, 10 (2004).
[28] G. L. Browning, J. J. Hack, and P. N. Swarztrauber Mon. Weather Rev. **117**, 1058 (1989).
[29] C. Ronchi, R. Iacono, and P. S. Paolucci, J. Comput. Phys. **124**, 93 (1996).
[30] R. Gómez, L. Lehner, P. Papadopoulos, and J. Winicour, Classical Quantum Gravity **14**, 977 (1997).
[31] J. Thornburg Classical Quantum Gravity **21**, 743 (2004).
[32] C. Reisswig, N. T. Bishop, C. W. Lai, J. Thornburg, and B. Szilágyi, Classical Quantum Gravity **24**, S237 (2007).
[33] R. Gómez, W. Barreto, and S. Frittelli, Phys. Rev. D **76**, 124029 (2007).
[34] H-O. Kreiss and J. Oliger, Methods for the approximate solution of time dependent problems, Global Atmospheric Research Program, Publication No. 10, World Meteorological Organization, Case Postale No. 1, CH-1211 Geneva 20, Switzerland.
[35] L. Lehner, J. Comput. Phys. **149**, 59 (1999).
[36] E. T. Newman and R. Penrose, J. Math. Phys. (N.Y.) **7**, 863 (1966).
[37] J. Winicour, J. Math. Phys. (N.Y.) **24**, 1193 (1983).
[38] J. Winicour, J. Math. Phys. (N.Y.) **25**, 2506 (1984).
[39] R. Gómez, Phys. Rev. D **64**, 024007 (2001).
[40] L. A. Tamburino and J. Winicour, Phys. Rev. **150**, 1039 (1966).
[41] J. Winicour, Gen. Relativ. Gravit. **19**, 281 (1987).
[42] N. T. Bishop, Classical Quantum Gravity **22**, 2393 (2005).
[43] J. N. Goldberg, A. J. MacFarlane, E. T. Newman, F. Rohrlich, and E. C. G. Sudarshan, J. Math. Phys. (N.Y.) **8**, 2155 (1967).
[44] Y. Zlochower, R. Gómez, S. Husa, L. Lehner, and J. Winicour, Phys. Rev. D **68**, 084014 (2003).